TÉCNICO LISBOA

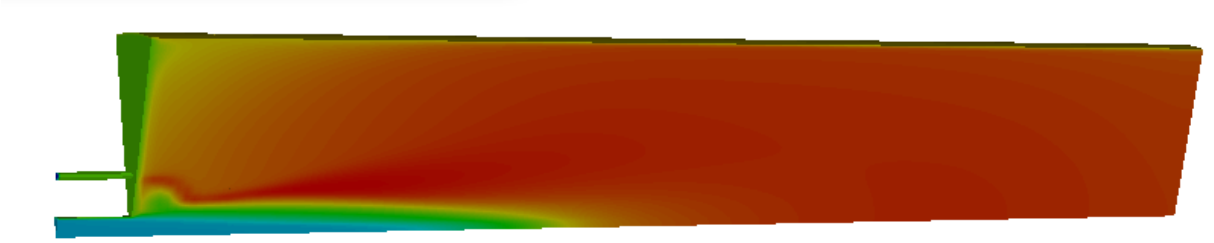

Numerical simulation of different combustion regimes in a laboratory combustor

Paweł Stanisław Rodak

Thesis to obtain the Master of Science Degree in

Energy Engineering and Management

Supervisor: Prof. Pedro Jorge Martins Coelho

Examination Committee

Chairperson: Prof. Edgar Caetano Fernandes

Supervisor: Prof. Pedro Jorge Martins Coelho

Member of the Committee: Prof. Daniel Cardoso Vaz

January 2017

“Stay hungry. Stay foolish.”

~ Steve Jobs

Acknowledgements

At first, I would like to thank Professor Pedro Coelho for his support in the development of this thesis. With his help and advice the accomplishment of this work was possible.

I would like to give credit to Adam Klimanek, Ph.D. Eng. for his valuable pieces of advice and comments concerning the ANSYS Fluent simulation.

Last, but not least, I wish to emphasize, that getting to the place I am today would not be possible without having the most loving family and Justyna, my marvelous girlfriend.

Abstract

The present dissertation reports the numerical simulations of a small-scale natural gas combustor operating in the flameless oxidation (FLOX) combustion regime, where the oxidation of the fuel occurs in an atmosphere with relatively low oxygen concentration. Such conditions are achieved as a result of the previous mixing between the preheated oxidizer, in this case, dry atmospheric air, and the combustion products. FLOX combustion regime is characterized by a distributed reaction zone, relatively uniform temperatures, no visible flame, low noise, low soot formation and in particular low NO_x emissions.

One configuration of the burner that is used to achieve flameless combustion regime consists of a central air nozzle, with the diameter of 10 mm, surrounded by 16 fuel nozzles, each with 2 mm diameter, situated at a distance of 15 mm from the center of the burner. Depending on the different configurations of the burner geometry, different combustion regimes may be observed. For this reason, the simulations have been performed for different burner configurations, to investigate their influence on the combustion process.

All the calculations have been performed using the ANSYS Fluent v17.1 code. Three grids, each with a different number of cells, have been built for the described above configuration in order to carry out the grid independence analysis and set down the approximate number of cells sufficient to perform further simulations. The influence of different burner geometry configurations on the combustion process has been investigated. These configurations differ on the diameter of the air nozzle and on the distance between the air and fuel nozzles.

The combustion model applied for all the simulations was the Eddy Dissipation Concept (EDC) coupled with the detailed chemical mechanism DRM-19. The turbulence model was $k-\omega$ SST. The results of simulations are presented. For the configurations corresponding to the experimental studies (A-E), numerical results have been compared to available measurement data. The configurations F-K were not tested experimentally nor numerically ever before.

The numerical results show that the applied turbulence model is not able to accurately predict the decay of the air stream at the vicinity of the burner. The simulations of different burner configurations show that for smaller air inlet diameters, the reaction zone moves progressively closer to the burner and due to more intense mixing, the temperature field is more leveled. A similar conclusion can be made for the smallest tested distance between air and fuel nozzles L = 7,5 mm. The combustion could be characterized by the flameless oxidation regime for this distance, with lower maximum temperature and more uniform temperature field, whereas for the fuel inlet distance of 30 mm, high temperature regions, indicating the presence of a flame front, were identified.

Resumo

A presente dissertação relata as simulações numéricas de uma câmara de combustão de gás natural de pequena escala operando no regime de combustão de oxidação sem chamas (FLOX), onde a oxidação do combustível ocorre em uma atmosfera com concentração de oxigênio relativamente baixa. Tais condições são conseguidas como resultado da mistura anterior entre o oxidante pré-aquecido, neste caso, ar atmosférico seco, e os produtos de combustão. O regime de combustão FLOX é caracterizado por uma zona de reacção distribuída, temperaturas relativamente uniformes, sem chama visível, baixo ruído, baixa formação de fuligem e em particular baixas emissões de NOxx.

Uma configuração do queimador que é utilizada para atingir o regime de combustão sem combustão consiste de um bocal central de ar, com o diâmetro de 10 mm, rodeado por 16 bicos de combustível, cada um com 2 mm de diâmetro, situado a uma distância de 15 mm do centro da O queimador. Dependendo das diferentes configurações da geometria do queimador, diferentes regimes de combustão podem ser observados. Por esta razão, as simulações foram realizadas para diferentes configurações de queimadores, para investigar sua influência no processo de combustão.

Todos os cálculos foram realizados usando o código ANSYS Fluent v17.1. Foram construídas três grelhas, cada uma com um número diferente de células, para a configuração acima descrita, a fim de realizar a análise de independência de grelha e definir o número aproximado de células suficientes para realizar simulações adicionais. A influência de diferentes configurações de geometria do queimador no processo de combustão tem sido investigada. Estas configurações diferem no diâmetro do bico de ar e na distância entre o ar e os bicos de combustível.

O modelo de combustão aplicado para todas as simulações foi o Eddy Dissipation Concept (EDC) acoplado com o detalhado mecanismo químico DRM-19. O modelo de turbulência foi k-ω SST. Os resultados das simulações são apresentados. Para as configurações correspondentes aos estudos experimentais (A-E), os resultados numéricos foram comparados com os dados de medição disponíveis. As configurações F-K não foram testadas experimentalmente nem numericamente antes.

Os resultados numéricos mostram que o modelo de turbulência aplicado não é capaz de prever com precisão o decaimento da corrente de ar na vizinhança do queimador. As simulações de diferentes configurações de queimador mostram que para diâmetros menores de entrada de ar, a zona de reação se move progressivamente mais perto do queimador e devido a mistura mais intensa, o campo de temperatura é mais nivelado. Uma conclusão semelhante pode ser feita para a menor distância testada entre o ar e os bicos de combustível L = 7,5 mm. A combustão poderia ser caracterizada pelo regime de oxidação sem chama para esta distância, com temperatura máxima mais baixa e campo de temperatura mais uniforme, enquanto que para a distância de entrada de combustível de 30 mm, foram identificadas regiões de alta temperatura, indicando a presença de uma frente de chama.

Keywords

- FLOX combustion regime
- Methane combustion
- ANSYS Fluent
- Numerical simulation
- DRM-19
- EDC

Palavras-chave

- Regime de combustão FLOX
- Combustão de metano
- ANSYS Fluent
- Simulação numérica
- DRM-19
- EDC

Index

Figures List

Tables List

Nomenclature

Roman Characters

Small Letters

a – Absorption coefficient (-)

$a_{\varepsilon,i}$ – Radiative blackbody emitted energy fraction (-)

a_1 – SST $k-\omega$ model constant (-)

g – Gravity acceleration vector (m^2/s)

h – Specific enthalpy (J/kg)

k – Turbulent kinetic energy (m^2/s^2)

l – Characteristic dimension (m)

m – Mass flow rate (kg/s)

m_i – Mass flow rate of species i (kg/s)

n – Refractive index (-)

p – Pressure (Pa)

$\vec{q}$ – Radiation heat flux vector (W/m^3)

q_R''' – Radiation heat flux energy source term (W/m^3)

$\vec{r}$ – position vector (m)

s – Path length (m)

$\vec{s}$ – Direction vector (m)

t – Time (s)

u – Velocity (m/s)

$\bar{u}$ – Average velocity (m/s)

u' – Fluctuating component of velocity

x – Position vector (m) or combustion chamber radial coordinate (m)

x_i – Position coefficient in direction i

x_j – Position coefficient in direction j

y – Distance to next surface (m)

γ_i – Mass fraction of species i (-)

z – Axial position vector (m)

Capital Letters

A_0 – Turbulence model parameter (-)

A_s – Turbulence model parameter (-)

C_1 – $k-\varepsilon$ model constant (-)

$C_{1\varepsilon}$ – $k-\varepsilon$ model constant (-)

C_2 – $k-\varepsilon$ model constant (-)

$C_{3\varepsilon}$ – $k-\varepsilon$ model constant (-)

Cp – Specific heat capacity at constant pressure (J/kgK)

C_{μ} – Turbulence model variable (-)

C_{ξ} – EDC model constant (-)

C_{τ} – EDC time scale constant (-)

C_{τ} – Time scale constant (-)

D – Diameter (m)

Da – Damköhler number (-)

D_i^M – Mass diffusivity coefficient of species i (m^2/s)

G_b – k source term relative to buoyancy effects (kg/ms^3)

G_{inc} – Incident radiation (W/m^2)

G_k – Production of turbulence kinetic energy (kg/ms^3)

G_{ω} – Generation of ω (kg/ms^3)

I – Radiative intensity (W/m^2)

$\vec{J_i}$ – Fick's law mass diffusion flux ($kg/(m^2s)$)

Le – Lewis number (-)

Re – Reynolds number (-)

$R_{i,r}$ – Rate of formation/destruction of species in reaction (kg/m^3s)

S – Strain rate magnitude (-)

S_{ij} – Strain rate tensor (1/s)

T – Temperature (K)

Y_i^* – Mass fraction of species i in the fine scales region (-)

Y_i^0 – Mass fraction of species i in the surrounding region (-)

V – Velocity (m/s)

Greek Characters

Small Letters

$\sigma_{k,1}$ –- SST $k-\omega$ model constant (-)

$\sigma_{\omega,1}$ – SST $k-\omega$ model constant (-)

$\sigma_{k,2}$ – SST $k-\omega$ model constant (-)

$\sigma_{\omega,2}$ – SST $k-\omega$ model constant (-)

$\beta_{i,1}$ – SST $k-\omega$ model constant (-)

$\beta_{i,2}$ – SST $k-\omega$ model constant (-)

δ_{ij} – Kronecker delta (-)

ε – Turbulent kinetic energy dissipation rate (m^2/s^3) or emissivity (-)

η – y direction cosine (-)

$\vec{\vartheta}$ – Velocity vector (m/s)

κ_i – Absorption coefficient of i – th grey gas (1/m)

λ – Thermal conductivity (W/(mK)) or excess air coefficient (-)

μ – Dynamic molecular viscosity (kg/ms) or z direction cosine (-)

μ_t – Turbulent viscosity (kg/(ms))

ν – Kinematic viscosity (m^2/s)

ξ – x direction cosine (-) or Mass fraction of the total fluid occupied by the fine structure regions (-)

ρ – Fluid density (kg/m^3)

σ – Stefan-Boltzmann constant ($W/(m^2K^4)$)

σ_ε – Turbulent kinetic energy dissipation rate Prandtl number (-)

σ_h – Energy Prandtl number (-)

σ_k – Turbulent kinetic energy Prandtl number (-)

σ_s – Scattering coefficient (-)

τ_{ij} – Viscous stress tensor (-)

ϕ – Transported scalar or turbulence model parameter or phase function (-)

ψ – Composition space vector (-)

ω – Specific turbulent kinetic energy dissipation rate (1/s)

$\dot{\omega}_i$ – Formation/destruction rate of chemical species i

Capital Letters

Γ_k – effective diffusivity of k (kg/ms)

Γ_ω – effective diffusivity of ω (kg/ms)

Ω' – Solid angle (-)

Ω_{ij} – Rate of rotation tensor (rad/s)

Exponents

$\left(\bar{\ }\right)$ – Reynolds time average

$\left(\tilde{\ }\right)$ – Favre mass-weighted average

$(\ )'$ – Reynolds fluctuation

$(\ )''$ – Favre fluctuation

$(\ )^0$ – Relative to the fine structure surroundings

$(\ )^*$ – Relative to the fine structures

Acronyms

CFD – Computational Fluid Dynamics

C-PDF – Joint Composition Probability Density Function

CPU – Central Processing Unit

DO – Discrete Ordinates

EDC – Eddy Dissipation Concept

EDM – Eddy Dissipation Model

FLOX – Flameless Oxidation

GHG – Green House Gas

GSCC – Gas-Steam Combined Cycle

HC – Hydrocarbon

HiTAC – High Temperature Air Combustion

ICCD – Intensified Charge Coupled Device

IEA – International Environmental Agency

ISAT – In-Situ Adaptive Tabulation

MILD – Moderate and Intense Low Oxygen Dilution

NO_x – Nitrogen Oxides

NS – Navier-Stokes

OECD – Organization for Economic Co-operation and Development

PDE – Partial Differential Equation

RAM – Random Access Memory

RANS – Reynolds Averaged Navier-Stokes

SST – Shear Stress Transport

WSGG – Weighted Sum of Gray Gases

Chapter 1

Introduction

1.1. Objective and Innovative Contribution of the Thesis

The key objective of this thesis is to investigate numerically the changes induced by the geometrical parameters of the small-scale combustor, namely the air nozzle diameter and the distance between the air and fuel nozzles, on the combustion process. For this purpose 11 configurations have been designed, namely A-K. For the configurations corresponding to the experimental studies (A-E) carried out in the previous work of Veríssimo et al. (2011), numerical results have been compared to available measurement data. The configurations F-K were not tested experimentally nor numerically ever before. The table 1.1 presents the different configurations.

Table 1.1 Simulated burner configurations.

Configuration	Air inlet diameter D_{air} (mm)	Air fuel inlets distance L (mm)
A	10	15
B	9	15
C	8	15
D	7	15
E	6	15
F	10	7.5
G	8	7.5
H	6	7.5
I	10	30
J	8	30
K	6	30

The innovative contribution involves the numerical study on the different configurations of the burner geometry of the small-scale combustor and its influence on the establishment of the flameless oxidation conditions. Furthermore, the eddy dissipation concept combustion model coupled with the DRM-19 chemical mechanism and SST $k-\omega$ turbulence model was not applied in the simulations of this particular combustor in past numerical studies.

1.2. Background and Motivation

Combustion of fuels has been, still is and will most probably remain for decades the main process for the production of energy in the World. As it can be seen in the figure below, falling into the context of this work, the use of natural gas as an energy source is rising significantly over the past years.

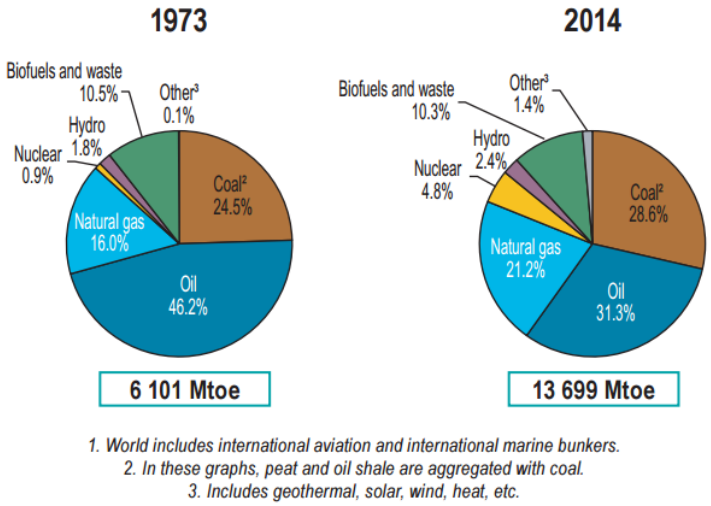

Fig. 1.1 Total primary energy supply by fuel (Key world energy statistics, IEA 2016).

The demand for energy has been rising since the beginning of civilization and will still be raising, as the developing countries such as China or India and others are rapidly growing their economies.

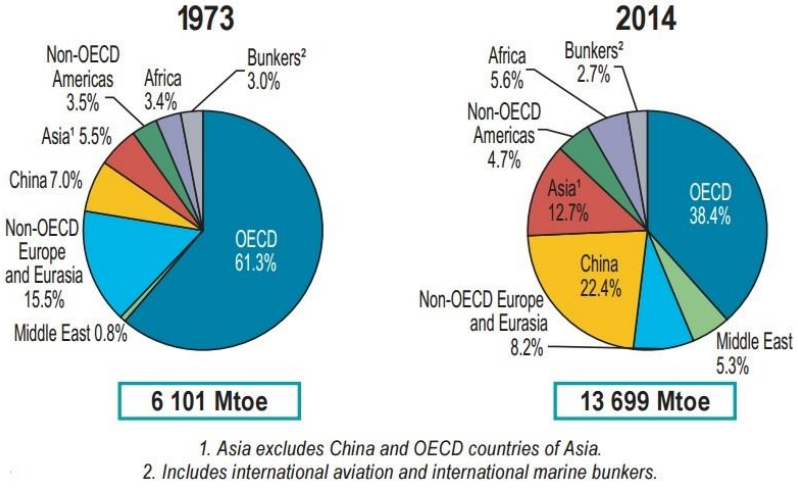

Fig. 1.2 Total primary energy supply by region (Key world energy statistics, IEA 2016).

The technology of combustion has been developed for decades, but still there are a demand and room for further improvement and innovation. This concerns especially the methods for reduction of greenhouse gas (GHG) emissions, pollutant emissions such as nitrous oxides (NO_x), carbon oxide (CO), soot, unburned hydrocarbons (HC) and improving the efficiency of the combustion process.

In this field the improvements can be achieved with the help of flameless oxidation (FLOX) combustion regime, also referred to as moderate or intense low oxygen dilution (MILD) combustion, colorless distributed combustion or high temperature air combustion (HiTAC). As it has been mentioned, the use of natural gas as a fuel is increasing. Natural gas is a fuel with several advantages over, for instance, coal. First of all, its combustion produces approximately 1.7 times less CO_2 per 1 kWh. Natural gas is cleaner by itself, easy to transport and has high energy density. It can be combusted in gas-steam combined cycle (GSCC) reaching efficiencies of about 60 %, which is much higher than state of the art coal power plants. Therefore the natural gas might become the fuel of the future, as the developed countries aim to reduce their emissions, improve the efficiency and become less dependent on coal. FLOX combustion is a very promising technology, which could be applied for instance in land based gas turbines, boilers combustion chambers and domestic heating systems (Cavaliere and Joannon 2004).

Studies like this one are an essential contribution to the knowledge about the FLOX combustion and also in the field of CFD numerical simulations.

1.3. FLOX Combustion Regime

The combustion regime is described in the literature by different names.

- FLOX – flameless oxidation
- MILD – moderate or low intense oxygen dilution
- HiTAC – high temperature air combustion
- Colorless distribution combustion
- Flameless combustion

It is a regime characterized by a volumetric reaction zone, more uniformed temperature field and the absence of a thin flame front. The oxidation of fuel occurs in an atmosphere with relatively low oxygen concentration, which is the effect of strong flue gas recirculation ratio. As a result, this combustion regime results in low noise, negligible soot formation, reduced NOx and CO emissions in comparison with regular combustion (Veríssimo et al. 2011). The regime is often achieved with the use of preheated air, however, this is not mandatory requirement as shown by Kumar et al. (2002), Krishnamurthy et al. (2009), and Mi et al. (2009). Due to the low oxygen concentration, the reaction develops slower and over a larger region comparing to the traditional combustion process.

This implies that the intensity of the reaction is strongly dependent on the speed of the reactions and therefore FLOX combustion cannot be simulated with the assumption of infinitely fast reactions. The characteristic fluid time and characteristic chemical reaction times are of the same order of magnitude. The Damköhler number (Da), defined by equation (1.4-1) takes a value of approximately 1.

$$Da = \frac{Characteristic\ fluid\ time}{Characteristic\ chemical\ reaction\ time} \sim 1 \qquad (1.4\text{-}1)$$

Figure 1.3 presents different combustion regimes on the graph of the relation between the temperature of reactants, oxygen concentration, dilutants (N_2+CO_2+H_2O) concentration and recirculation ratio. As it has been mentioned, FLOX combustion occurs in conditions with a high temperature of reactants and under low oxygen concentrations.

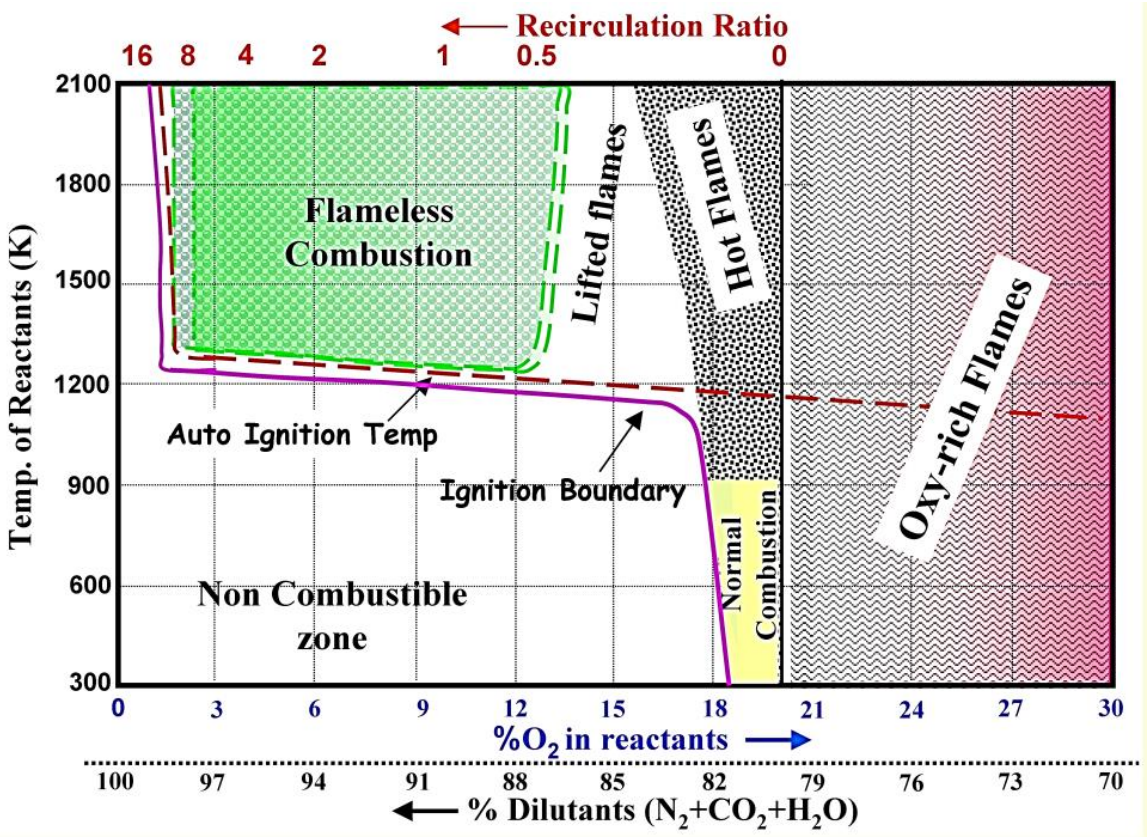

Fig. 1.3 Different combustion regimes presented on the graph of the relation between the temperature of reactants, oxygen concentration, dilutants (N_2+CO_2+H_2O) concentration and recirculation ratio (Source: www.intechopen.com/source/html/45115/media/image13.png).

Flameless combustion initially was developed to suppress the thermal mechanism of NO_x formation in burners for heating industrial furnaces using preheated combustion air. Without the technology, maintaining the acceptable levels of NO_x emission would not be possible in many cases. The technique is applied in multiple installations now, for instance in the steel industry. There are a lot of new applications being researched (Wünning and Wünning 2001).

Recent applications of FLOX combustion include the research and development of gas turbines and gasification systems, boiler combustion chambers and domestic heating systems. It can be specifically valuable for gas turbine applications due to low maximum temperatures, close to the temperatures at the inlet of a gas turbine, low noise operation, flame stability and reduced pollutant emissions (Noor et al. 2012). The flameless combustion is one of the most promising technologies that can meet the strictest regulations for reduced pollution and increased efficiency in gas turbines of the future (Veríssimo et al. 2013). Despite its potential, the technology is still not widely applied in industrial applications.

Although FLOX combustion was discovered decades ago, the current knowledge is still limited. Therefore studies like this one are an important contribution to this promising field of combustion knowledge.

1.4. Modeling the Combustion Process with Computational Fluid Dynamics (CFD)

Fluid flows are governed by partial differential equations (PDE), which are the representation of conservation laws for mass, momentum and energy. CFD aims to replace such PDE systems by sets of algebraic equations which can be solved by computers.

CFD enables to perform the numerical simulations, which allow getting an insight into flow patterns, that are difficult, expensive or impossible to study using experimental techniques. With the increasing capacity of modern computers, this branch of knowledge is expected to grow rapidly. CFD does not replace the measurements completely, for instance in this study the experimental data are useful to verify the results of the calculations. Thanks to CFD, the number of measurements can be significantly reduced. Numerical simulations are cheaper, faster and can be applied to a wide range of purposes, while experiments are usually built for one or few very specific cases.

Modeling of combustion is a very complex problem in CFD simulations. It requires a high level of expertise and combines multiple fields of knowledge such as:

- Fluid dynamics
- Chemistry (stoichiometry, thermochemistry, equilibrium)
- Thermodynamics (heat transfer, radiation)
- Applied mathematics

The aspects affecting the methods chosen for the simulation of the combustion process are:

- Kinetic/diffusion combustion

- Laminar/turbulent combustion
- Global/detailed chemical reactions
- Interaction of turbulence and chemical reactions
- Steady / unsteady conditions
- Single / multiple phases flows
- The possibility to introduce simplifications
- The available computing power

Modeling of combustion is indispensable in modern science and engineering as it serves in fields of design, verification, testing, and optimization. As it was stated in chapter 1.1., the combustion of fuels will long remain the main process for the production of energy in the World. Furthermore, some applications of combustion are nowadays impossible to substitute, for instance in the propulsion of rockets or in commercial aviation.

Taking into consideration the flameless combustion and its characteristics when it comes to setting up the numerical simulation, all the detailed information are elaborated in chapter 3. In the present simulation, available computing power turned out to have a strong influence on the form that the simulation has taken. All the work has been performed on a personal computer equipped with Intel Core i5-3230M CPU @ 2.6 GHz (2 cores, 4 threads) and 8 GB of RAM. Relatively modest available computing power was, in this case, the motivation to seek the simplest model, that would be able to satisfactory predict the measure data and make it possible to run multiple simulations with different burner configurations, which is the key objective of this dissertation. Available computing power impacts practically every step of building the model, beginning with simplification of geometry, deciding about the appropriate number of mesh cells, the choice of turbulence model, combustion model, and reaction mechanism.

1.5. Literature Overview

1.5.1. Introduction

The present work draws from the knowledge collected through the decades of studies on flameless combustion and numerical CFD simulations. Moreover, it is an extension of experiments performed on the simulated combustor, referred to as small-scale combustor or laboratory combustor.

In this section available scientific studies concerning the present dissertation will be presented in separate chapters:

- In the chapter 1.4.2. the studies concerning the combustion regime
- In the chapter 1.4.3. the studies concerning the research work related to the small-scale combustor

- In the chapter 1.4.4. the studies concerning the numerical simulations of flameless combustion regime

1.5.2. FLOX Combustion Regime

Wünning and Wünning (1997) used experimental and numerical techniques to find out if the mild combustion regime is able to lower NO_x emissions. The study concluded that such effect is indeed achieved through lowered adiabatic flame temperatures, so by the inhibition of the thermal mechanism of NO_x formation.

Katsuki and Hasegawa (1998) reviewed the advances in heat recirculating combustion in industrial furnaces. The authors concluded that using pre-heated air leads to higher efficiency and thus higher energy savings.
Furthermore, their conclusion was that the dilution of the air with flue gasses and combustion occurring with low oxygen concentration are indispensable factors in the achievement of low NO_x emissions.

Noor et al. (2012) provided the review and discussion of recent research concerning the flameless oxidation combustion. The authors show that the flameless oxidation can be nowadays successfully applied in closed furnaces. The preheating of the air may not be necessary because a closed furnace can self-preheat the supplied air and self-dilute the oxygen in the combustion chamber. The authors conclude, that flameless combustion produces greater efficiency with lower emissions comparing to the traditional combustion. What is more, the use of biogas should be considered, as it would close the natural CO_2 cycle and would not contribute to the greenhouse gas emission.

1.5.3. Small-scale Combustor

Veríssimo et al. (2011) examined experimentally the operational, combustion and emission characteristics of the small-scale combustor. The combustion characteristics were measured as a function of the excess air coefficient (λ). For low values of λ, the flameless combustion was achieved and for the values of λ over 1.5 the conventional lean combustion was observed. The authors conclude, that the present combustor yields very low NO_x and CO emissions which was attributed to the suppression of thermal mechanism introduced by the flameless oxidation and lean combustion modes.

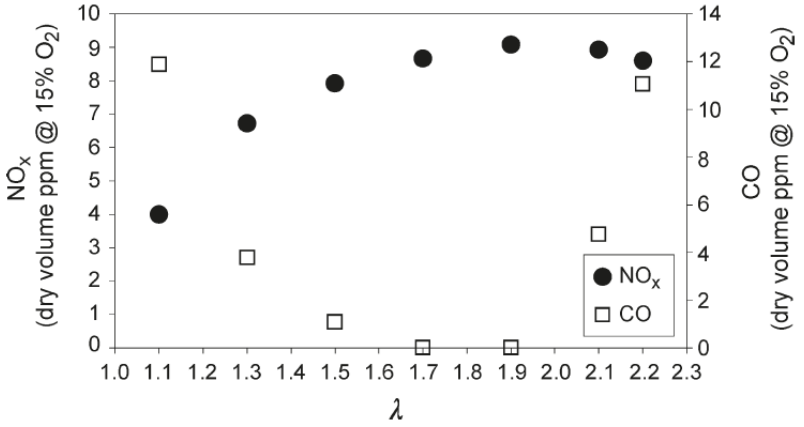

Fig. 1.4 NO_x and CO emissions as a function of the excess air coefficient (Veríssimo et al. 2011).

Veríssimo et al. (2013) using the same small-scale combustor examined the influence of the thermal input on the operation of the combustor working under flameless oxidation conditions. The results of their work show that as the thermal input increases, the main reaction zone enlarges and moves progressively closer to the combustor exit as a result of the increase in the central jet momentum. For all the configurations, the combustor produced very low NOx and CO emissions, however, the CO emission was rising along with higher thermal inputs, presumably because of lower residence times associated with higher thermal loads. The authors conclude that good performance of the combustor when it comes to the level of emissions was achieved because the combustor operated under the flameless oxidation combustion regime.

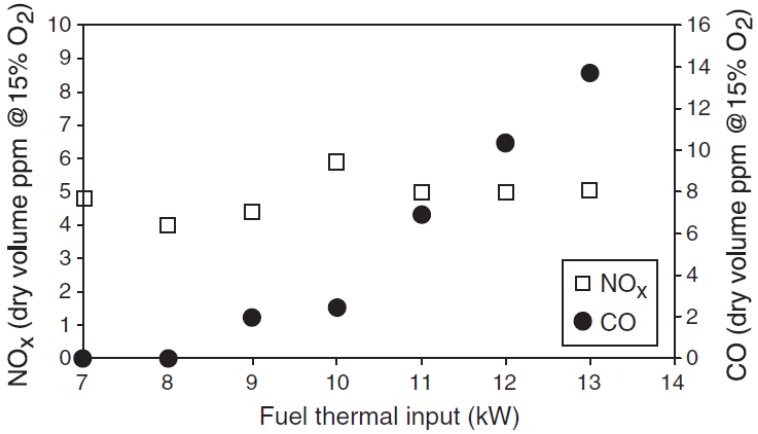

Fig. 1.5 NO_x and CO emissions as a function of the fuel thermal input (Veríssimo et al. 2013).

Veríssimo et al. (2013) performed another study on the small-scale combustor, aimed to probe the importance of the air inlet velocity on the establishment of flameless combustion conditions. The variation of the air inlet velocity was achieved as a result of changing the air nozzle diameter while keeping constant power level. The researchers found out that the flameless combustion occurs regardless of the air inlet velocity for the λ = 1.3, whereas for λ > 1.7 the establishment of flameless oxidation conditions was not possible for all studied air jet momentums. The conclusion of the study was that for future gas turbines with similar burner design, the establishment of flameless oxidation conditions might be problematic.

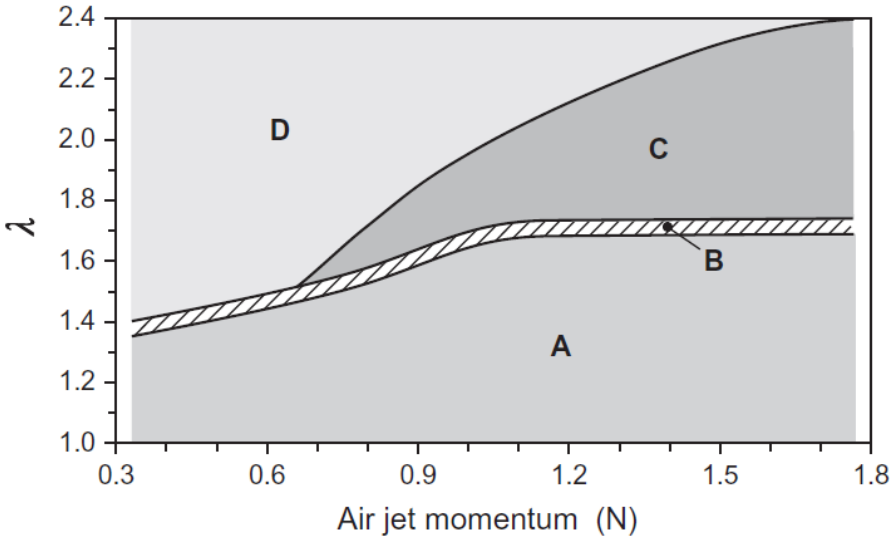

Fig. 1.6 Combustion regime regions identified in the present combustor operating with a thermal load of 10 kW and an inlet air temperature of 673 K. (A) Flameless combustion, (B) transition region, (C) visible flame and (D) no combustion (Veríssimo et al. 2013).

1.5.4. Numerical Studies

Christo and Dally (2005) performed numerical simulations of an open flame using different turbulence and combustion models. The authors concluded that the standard $k-\varepsilon$ model with $c_{1\varepsilon}$ constant set to 1.6 leads to more satisfactory results. The other conclusion was that Eddy Dissipation Concept (EDC) with detailed chemical mechanism successfully predicted the results obtained by experiments.

Graça et al. (2012) conducted the numerical simulation of reversed flow small-scale combustor. Natural gas was used as a fuel and air was preheated to 600 K. By changing the air flow, two conditions were achieved, namely conventional lean combustion and flameless combustion. The simulation was carried out using ANSYS Fluent v13 code. Turbulence was modeled by $k-\varepsilon$ model. Two combustion models were employed, namely the EDC and the combustion PDF (C-PDF) models. Good agreement between the predictions obtained using the two combustion models was found in comparison to the available experimental data. Both models were found to underpredict the measured temperature in the vicinity of the axis in the region close to the burner, meaning that the main combustion zone is delayed comparing to the experimental data.

Hosseini et al. (2014) analyzed the combustion characteristics of biogas flameless mode. ANSYS Fluent code was used to perform the simulation. Two combustion modes were compared, the conventional mode and flameless combustion mode. For modeling of the combustion, the two step reaction scheme with eddy dissipation model (EDM) was implemented and for turbulence modeling, the standard $k-\varepsilon$ model was applied. The authors concluded that the flameless combustion mode produces smaller NO_x emissions comparing to the conventional mode due to more uniform temperature. The another conclusion was that very high concentration of CO_2 in biogas flameless combustion causes higher heat capacity and better radiation heat transfer in the system.

Veríssimo et al. (2015) in a recent study compared the available experimental data with the results of the simulation of the combustion process within the small-scale combustor. The calculations were carried out using the commercial code ANSYS Fluent. Turbulence model was the realizable $k-\varepsilon$ model and the chemical reactions were simulated with the eddy dissipation concept coupled with either skeletal chemical mechanism incorporating 13 chemical species and 73 chemical reactions or a global single-step reaction mechanism. The simulation revealed that more complex chemical mechanisms manage to accurately predict the temperature and the concentrations of CO_2 and O_2 over most of the combustor length. Nevertheless, the temperature field was overestimated in the vicinity of the burner and discrepancies were found in the prediction of CO concentration.

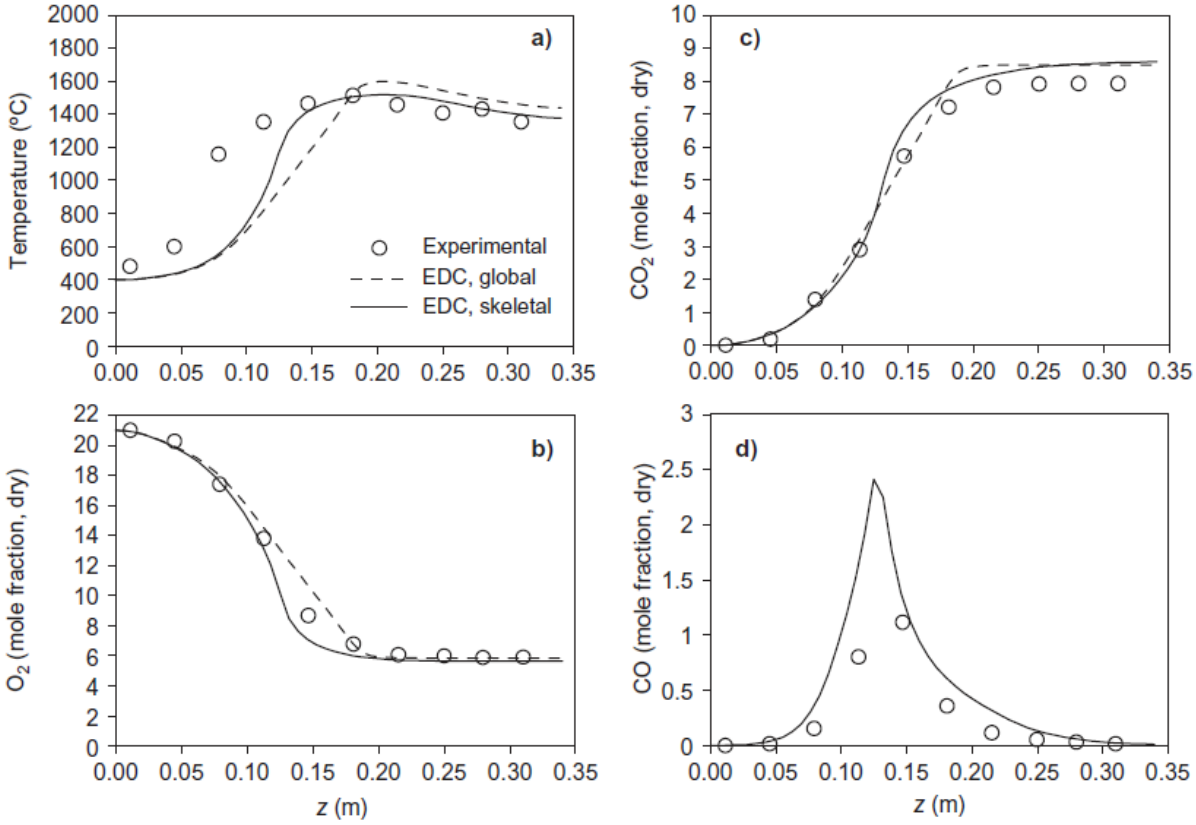

Fig. 1.7 Predicted and measured axial profiles of mean temperature and O_2, CO_2, and CO concentrations for the thermal load of 10 kW and an inlet air temperature of 673 K (Veríssimo et al. 2015).

Chapter 2

Experimental Installation

2.1. Introduction

The purpose of this chapter is to give an insight into the experimental setup, which was applied in order to produce the experimental results for configurations A-E. It needs to be stressed, that the experiment has been performed in past study of Veríssimo et al. (2011). For the needs of the present study, only the numerical simulations were carried out.

This chapter contains the description of the analyzed installation, the small-scale combustor. Firstly the construction of the given combustor is presented and subsequently, the measurement setup, which has been applied in order to obtain the experimental data.

2.2. Small-scale Combustor

Figure 2.1 shows a schematic of the combustor simulated in this study. The combustion chamber is a quartz glass cylinder with an inner diameter of 100 mm and a length of 340 mm. The quartz cylinder is insulated with a 30 mm thick ceramic fiber blanket.

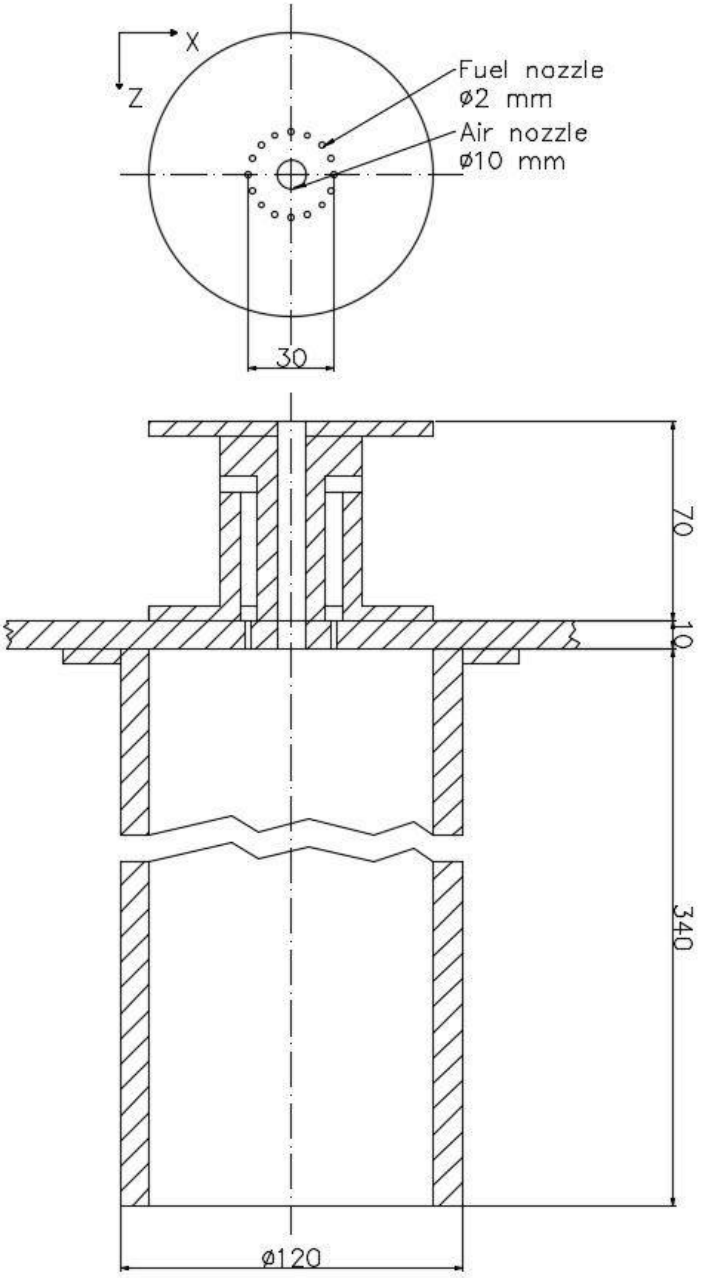

Fig. 2.1 Schematic of the combustor.

The burner is placed at the top end of the combustion chamber and the exhaust of the burned gasses is made by the bottom end. As seen in figure 2.1, the burner consists of a central orifice with 10 mm inner diameter, through which the combustion air is supplied, surrounded by 16 small orifices of 2 mm inner diameter each, positioned on a circle with a radius of 15 mm, for the fuel (methane) supply. The combustion air is preheated by an electrical heating system that allows air inlet temperatures up to 700°C.

The central orifice has an adjustable inner diameter. In the study of Veríssimo et al. (2013), different settings were analyzed. Changing the air inlet diameter, while maintaining constant excess air coefficient λ and constant power level, results in changes of the air inlet velocity.

Table 2.1 describes the different configurations of air inlet diameter and velocity. All the parameters were calculated on the basis of the data provided by table 2.2. The same parameters were set in the numerical model described in chapter 4.

Table 2.1 Experimental burner configurations.

Configuration:	Air inlet diameter, D_{air} [mm]:	Air inlet velocity (normal), V_{air} [m/s]:
A	10	108.47
B	9	133.92
C	8	169.49
D	7	221.37
E	6	301.31

Predictions for these different settings have also been simulated and compared with available experimental data. For all the configurations presented in table 2.1, the parameters in table 2.2. remained constant.

Table 2.2 Experimental conditions.

Parameter:	Value:
Fuel composition (molar fractions):	1 CH_4
Air composition (molar fractions):	0.21 O_2, 0.79 N_2
Input power (kW):	10
Pressure, p (kPa):	101,3
Fuel temperature, T_{fuel} (K):	298
Air temperature, T_{air} (K):	673
Excess air coefficient, λ (-):	1.3
Fuel inlet diameter, D_{fuel} (mm):	2
Fuel inlet velocity (normal) V_{fuel} (m/s):	6.06

2.3. The Measurement Setup

Local mean temperature measurements were obtained using R type thermocouples. The uncertainty due to radiation heat transfer was estimated to be less than 5% by considering the heat transfer by convection and radiation between the thermocouple bead and the surroundings. The sampling of the gasses for the measurement of local mean O_2, CO_2, HC, CO, and NO_x concentrations was achieved using a stainless-steel, water-cooled probe. The analytical instrumentation included a magnetic pressure analyzer for O_2 measurements, a non-dispersive infrared gas analyzer for CO_2 and CO measurements, a flame ionization detector for HC measurements and a chemiluminescent analyzer for NO_x measurements. On average, the repeatability of the gas species concentration data was within 10% of the mean value.

Flue-gas composition data was obtained using the procedures described above for the concentration measurements inside the combustor. Repeatability of the flue-gas data was, on average, within 5% of the mean value. Both the temperature and the gas species probes were inserted into the quartz-glass combustion chamber through holes made on the bottom end of the combustor.

The measurement points are presented in figure 2.2. For all the measurement points, the data include:

- Temperature
- Species concentrations: NO_x, CO, CO_2, O_2

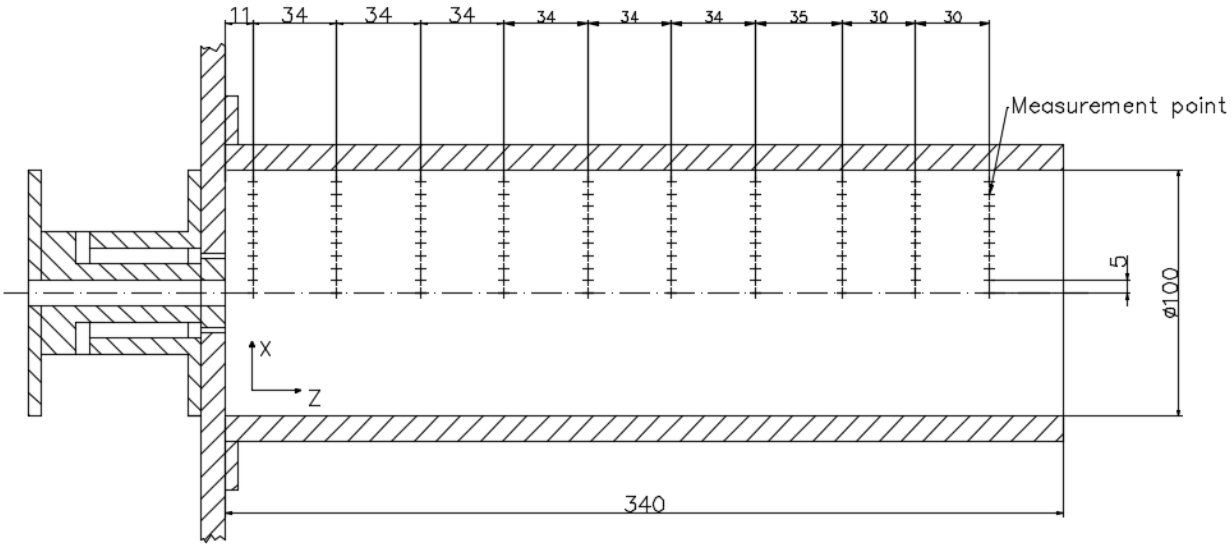

Fig. 2.2 Schematic of the combustor with the measurement points overlaid.

In order to monitor the main combustion zone inside the combustor, the chemiluminescence imaging was performed in the study of Veríssimo et al. (2011). This technique aims to record the light emitted from the chemically excited OH, denoted OH*, which is an important intermediate species in the oxidation of hydrocarbon fuels. The OH radical is formed in the flame front, and this is why OH is a commonly used marker for this region.

The OH* images were collected on an ICCD camera (FLAMESTAR II, LaVision, 286 384 pixels), equipped with a UV lens (UV Nikkor, 105 mm, f/4.5) and a bandpass interference filter (Melles Griot) centered at 310 nm with a bandwidth of 10 nm. To eliminate the dark signal, background images were taken with capped camera, under the same integration time and gain of the measured images, for subsequent subtraction from the originally measured images. In all chemiluminescence experiments, 500 single instantaneous images were recorded and averaged. The ICCD camera collected the signal from the entire combustion chamber so that the signals were spatially integrated in depth. To obtain local information instead of line-of-sight information, each averaged OH* image was subsequently tomographically reconstructed using the inverse transform of Abel. Repeatability of the photometric data was, on average, within 5% (Veríssimo et al. 2011).

Chapter 3

Mathematical Model

3.1. Introduction

In this chapter, all the details concerning the mathematical model are collected. The equations solved and chemical mechanism are described.

The description of the reactive flow requires the solution of the following equations:

- Conservation of mass (continuity equation)
- Conservation of momentum
- Conservation of energy
- Conservation of every species involved
- The equations of the turbulence model

Initially, the conservation equations of mass, momentum, and energy are presented. Their equations are averaged in time yielding the Reynolds-Averaged Navier-Stokes equations (RANS). Secondly, the turbulence models, Shear Stress Transport (SST) $k-\omega$ model (Menter 1993), which was applied in all the simulation cases, and the realizable $k-\varepsilon$ model (Shih et al. 1995) are presented. The realizable $k-\varepsilon$ turbulence model has been used in the simulation of configuration A (described in part 2.1.) to compare the two turbulence models. Following this, the combustion Eddy Dissipation Concept (EDC) model (Magnussen 1981) and the reaction mechanism DRM-19 (Kazakov and Frenklach) are described. Finally, the Discrete Ordinates (DO) model, which was used to calculate the radiation source term of the energy equation, is presented.

3.2. Conservation Equations for Flows with Reactions

In this part, the conservation equations for mass, momentum, and energy are described.

The equation of mass conservation:

$$\frac{\partial \rho}{\partial t} + \nabla \cdot \left(\rho \, \vec{\vartheta}\right) = 0 \tag{3.2.-1}$$

where ρ represents the fluid density, t the time, $\vec{\vartheta}$ the velocity vector.
Under the assumption, that diffusion flux is given by Fick's law, the equation of mass conservation of species i has the following form:

$$\frac{\partial (\rho \gamma_i)}{\partial t} + \nabla \cdot \left(\rho \, \vec{\vartheta}_i \, \gamma_i\right) = -\nabla \cdot \vec{J_\iota} + \dot{\omega}_i \tag{3.2.-2}$$

Fick's law of diffusion:

$$\vec{J_\iota} = -D_i^M \rho \nabla \gamma_i \tag{3.2.-3}$$

where γ_i represents the mass fraction of species i, D_i^M the molecular diffusion coefficient of chemical species i, $\dot{\omega}_i$ the rate of production or consumption of chemical species i related to the chemical reactions.

The equation of momentum conservation (for Newtonian fluid):

$$\rho \frac{\partial \, \vec{\vartheta}}{\partial t} + \rho \, \vec{\vartheta} \cdot \nabla \, \vec{\vartheta} = -\nabla \mathrm{p} + \nabla \cdot \left[\mu \left[\nabla \, \vec{\vartheta} + \left(\nabla \, \vec{\vartheta}\right)^T\right] - \frac{2}{3}\mu \left(\nabla \cdot \vec{\vartheta}\right)\delta_{ij}\right] + \rho \vec{g} \tag{3.2.-4}$$

where p represents the pressure, μ the dynamic molecular viscosity, $\vec{g}$ the gravity acceleration vector, δ_{ij} the Kronecker symbol (which takes values $\delta_{ij} = 1$ if $i = j$ and $\delta_{ij} = 0$ if $i \neq j$).

The equation of energy conservation (in terms of specific enthalpy, at constant pressure, neglecting viscous dissipation and assuming that for all species i the thermal diffusivity is equal to mass diffusivity, $Le = 1$):

$$\frac{\partial\,(\rho h)}{\partial t} + \nabla \cdot (\rho\,\vec{\vartheta}\,h) = \nabla \cdot \left[\frac{\lambda}{Cp}\nabla h\right] + q_R'''$$

(3.2.-5)

where h is the specific enthalpy, λ the thermal conductivity, Cp the specific heat capacity at constant pressure, q_R''' the heat exchange by radiation.

3.3. Turbulence in Reactive Flows

In turbulent combustion, the turbulence and reactions influence one another. Combustion is a very complex phenomenon by itself. The reactions can be characterized by significant range of time and spatial scales. Complete description requires the solution of a large number of reaction equations and chemical species transport equations. Turbulence modeling is one of the most difficult CFD problems. It is also characterized by substantial variations in time and spatial scales, from scales of the range of the analyzed system down to Kolmogorov scales.

The simulation of turbulent reactive flows requires two-way interaction of turbulence and chemical reactions. Turbulence impacts the combustion process occurring within the flow and, on the other hand, the chemical reactions may produce or suppress turbulence.

Characteristics of turbulence:

- Irregularity

All the turbulent flows are characterized by the irregularity of flow variables, which makes it necessary to use statistical analysis.

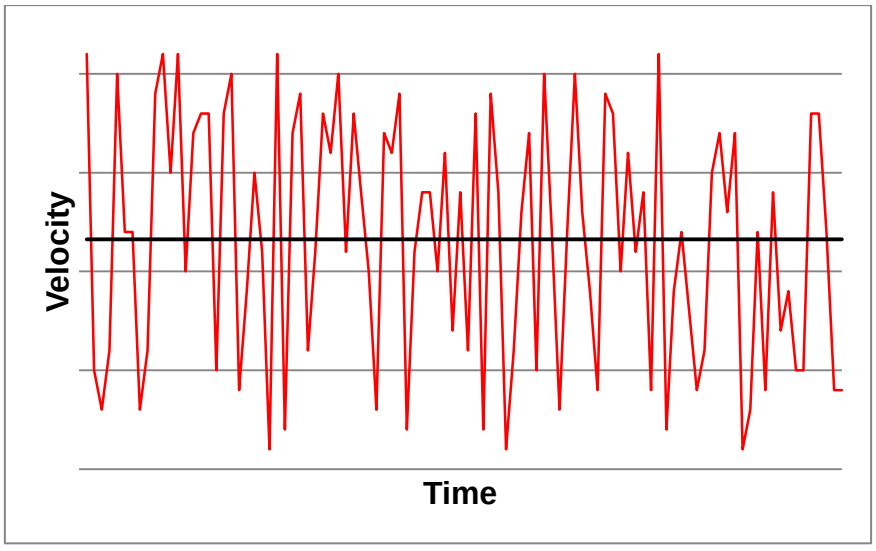

Fig. 3.1 The variations of velocity in time caused by turbulence (example).

- Diffusivity

It intensifies the exchange of heat, momentum, and mass in turbulent flows by causing intensive mixing.

- Large Reynolds number

Turbulent flows are characterized by large Reynolds numbers. The Reynolds number (Re) can be calculated from the equation:

$$Re = \frac{Vl}{\nu} \tag{3.3.-1}$$

where V is the velocity magnitude, l the characteristic dimension (diameter for flow in pipes) and ν the kinematic viscosity.

For instance, the Reynolds number calculated at the air inlet for configuration A is equal to:

$$Re = 17\,192.9 \tag{3.3.-2}$$

Values of $Re > 10\,000$ indicate that the flow is fully turbulent.

- Three-dimensional
- Multiple scales

Turbulence is observed in all scales. Beginning with the smallest swirls, where the mechanical energy is transformed into heat up to swirls of the meters range (for technical flows).

- Strong dissipativity

Viscous forces do work by transforming kinetic energy of the flow into heat. Therefore, maintaining turbulence requires the continuous supply of energy. Without a source of energy, turbulence is quickly suppressed and decays.

The description of a flow requires the solution of the set of Navier-Stokes (NS) equations. The NS equations in their full form are not practical for direct application to common engineering problems. For this reason, Reynolds Averaged Navier-Stokes (RANS) equations may have to be implemented, especially for the purpose of turbulence modeling.

The Navier-Stokes equations have the following form:

$$\rho\frac{\partial u_i}{\partial t}+\rho\frac{\partial u_i u_j}{\partial x_j}=-\frac{\partial p}{\partial x_i}+\frac{\partial}{\partial x_j}\left(\mu\left(\frac{\partial u_i}{x_j}+\frac{\partial u_i}{x_i}-\frac{2}{3}e^k\frac{\partial u_k}{\partial x_k}\right)\right)$$

(3.3.-3)

where u is the velocity and x is the position vector.

The basic tool for the derivation of the RANS equations from NS equations is the Reynolds decomposition. Reynolds decomposition of the flow variable, for instance, the velocity u is as follows. The graphical interpretation of the Reynolds decomposition is presented in the figure 3.2.

$$u=\bar{u}+u'$$

(3.3.-4)

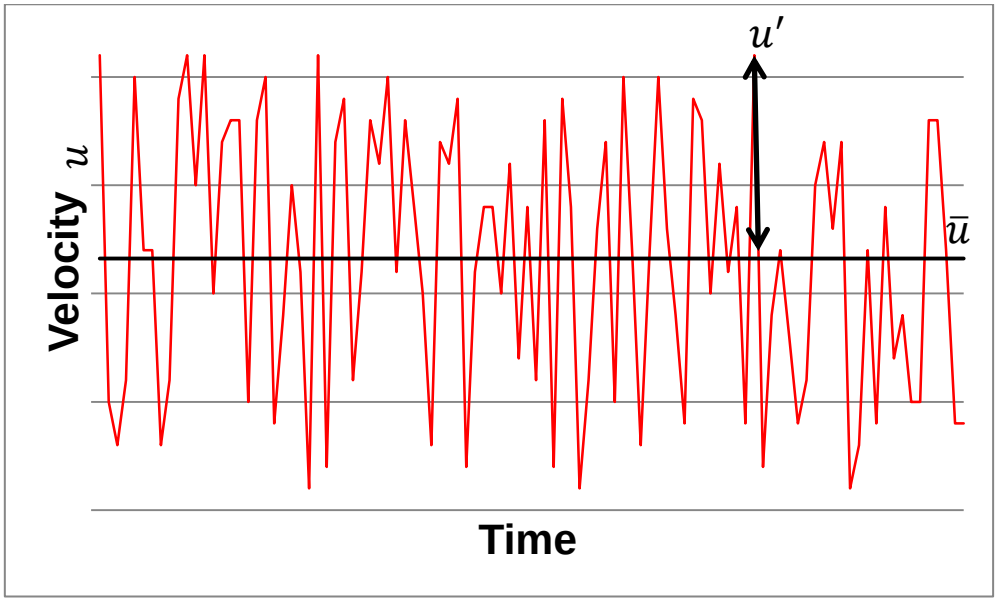

Fig. 3.2 Instantaneous velocity graph with the averaged velocity line and the fluctuating component (example).

Where $\bar{u}$ is the average velocity and u' is the fluctuating component. In Reynolds decomposition, the fluctuating component has the following property.

$$\overline{u'}=0$$

(3.3.-5)

Reynolds Averaged Navier-Stokes equations have the following form:

$$\bar{\rho}\frac{\partial \bar{u}_i}{\partial t}+\bar{\rho}\frac{\partial}{\partial x_j}\left(\bar{u}_i\bar{u}_j+\overline{u_i'u_j'}\right)=-\frac{\partial \bar{p}}{\partial x_i}+\frac{\partial}{\partial x_j}\left(\mu\left(\frac{\partial \bar{u}_\iota}{x_j}+\frac{\partial \bar{u}_\iota}{x_i}-\frac{2}{3}e^k\frac{\partial u_k}{\partial x_k}\right)\right)$$

(3.3.-6)

After the averaging, the component $\rho\overline{u_i'u_j'}$ appears in the equation, which is called the Reynolds Stresses.

In combustion problems, the continuity equations must include density variation. Therefore a density-weighted average velocity, called Favre average is introduced:

$$u = \tilde{u} + u''$$

(3.3.-7)

where:

$$\tilde{u} = \frac{\overline{\rho u}}{\bar{\rho}}$$

(3.3.-8)

It should be noted, that in Favre averaging, the time average of the fluctuations is not equal to zero:

$$\overline{u''} \neq 0$$

(3.3.-9)

Falling into the context of turbulence modeling, RANS models offer the most economic approach for computing complex turbulent flows. $k-\varepsilon$ (Launder and Spalding 1974) and $k-\omega$ (Wilcox 1986) are among the most commonly used turbulence models. These models simplify the problem of turbulence calculation to the solution of two additional transport equations and introduce Eddy-Viscosity (turbulent viscosity) to compute the Reynolds Stresses.

3.4. SST $k-\omega$ Turbulence Model

Two equation models, such as $k-\varepsilon$ and $k-\omega$ are the most widely applied ones for modelling turbulence in CFD for industrial applications. They solve two transport equations and model Reynolds Stresses using the Eddy Viscosity Approach.

SST (Shear Stress Transport) $k-\omega$ (Menter 1993) model combines the advantages of $k-\varepsilon$ and $k-\omega$ models. The significant advantage of $k-\omega$ over $k-\varepsilon$ model is better representation of turbulence in near wall region. Furthermore, the addition of the SST formulation means that it is characterised by small sensitivity to inlet conditions of quantities describing the turbulence. It is a desired characteristic due to the fact that usually such quantities are not well known, which is also the case in the present study.

In the two equation model $k-\omega$, the first transported variable is turbulent kinetic energy k, which determines the energy in the turbulence. The second transported variable is the specific dissipation ω, which determines the scale of the turbulence.

Transport equations for SST $k-\omega$ model are as follows.

$$\frac{\partial}{\partial t}(\rho k)+\frac{\partial}{\partial x_i}(\rho k u_i)=\frac{\partial}{\partial x_j}\left(\Gamma_k \frac{\partial k}{\partial x_j}\right)+G_k-Y_k+S_k \tag{3.4.-1}$$

$$\frac{\partial}{\partial t}(\rho \omega)+\frac{\partial}{\partial x_j}\left(\rho \omega u_j\right)=\frac{\partial}{\partial x_j}\left(\Gamma_\omega \frac{\partial \omega}{\partial x_j}\right)+G_\omega-Y_\omega+D_\omega+S_\omega \tag{3.4.-2}$$

In these equations, the term G_k represents the production of turbulence kinetic energy, and is defined in the same manner as in the standard $k-\omega$ model. G_ω represents the generation of ω, calculated as described below. Γ_k and Γ_ω represent the effective diffusivity of k and ω, respectively, which are calculated as described below. Y_k and Y_ω represent the dissipation of k and ω due to turbulence. D_ω represents the cross-diffusion term (S_k and S_ω are user-defined source terms, which are equal to zero in the present work).

The term G_k represents the production of turbulence kinetic energy. From the exact equation for the transport of k, this term may be defined as:

$$G_k=-\rho\overline{u_i' u_j'}\frac{\partial u_j}{\partial x_i} \tag{3.4.-3}$$

The model consists in calculation of the Reynolds stress tensor, $\rho\overline{u_i' u_j'}$, which is calculated as follows:

$$-\rho\overline{u_i' u_j'}=\mu_t\left(\frac{\partial u_i}{\partial x_j}+\frac{\partial u_j}{\partial x_i}\right)-\frac{2}{3}\delta_{ij}\left(\rho k+\mu_t\frac{\partial u_k}{\partial x_k}\right) \tag{3.4.-4}$$

In the SST $k-\omega$ model, the production of ω is given by:

$$G_\omega=\alpha\frac{\omega}{k}G_k \tag{3.4.-5}$$

where α is defined by:

$$\alpha = \frac{\alpha_\infty}{\alpha^*}\left(\frac{\alpha_0 + \frac{Re_t}{R_k}}{1 + \frac{Re_t}{R_k}}\right) \tag{3.4.-6}$$

$$\alpha^* = \alpha^*_\infty\left(\frac{\alpha^*_0 + \frac{Re_t}{R_k}}{1 + \frac{Re_t}{R_k}}\right) \tag{3.4.-7}$$

$$Re_t = \frac{\rho k}{\mu\omega} \tag{3.4.-8}$$

$$R_k = 6 \tag{3.4.-9}$$

$$\alpha^*{}_0 = \frac{\beta_i}{3} \tag{3.4.-10}$$

$$\beta_i = 0.072 \tag{3.4.-11}$$

$$\alpha^*{}_\infty = F_1\alpha^*{}_{\infty,1} + (1 - F_1)\alpha^*{}_{\infty,2} \tag{3.4.-12}$$

$$\alpha^*{}_{\infty,1} = \frac{\beta_{i,1}}{\beta^*_\infty} - \frac{\kappa^2}{\sigma_{\omega,1}\sqrt{\beta^*_\infty}} \tag{3.4.-13}$$

$$\alpha^*{}_{\infty,2} = \frac{\beta_{i,2}}{\beta^*_\infty} - \frac{\kappa^2}{\sigma_{\omega,2}\sqrt{\beta^*_\infty}} \tag{3.4.-14}$$

F_1 and F_2 are given by:

$$F_1 = \tanh(\Phi_1^4) \tag{3.4.-15}$$

$$\Phi_1 = \min\left[\max\left[2\frac{\sqrt{k}}{0.09\omega y}, \frac{500\mu}{\rho y^2 \omega}\right], \frac{4\rho k}{\sigma_{\omega,2} D_\omega^+ y^2}\right]$$

(3.4.-16)

$$D_\omega^+ = \max\left[2\rho\frac{1}{\sigma_{\omega,2}}\frac{1}{\omega}\frac{\partial k}{\partial x_j}\frac{\partial \omega}{\partial x_j}, 10^{-10}\right]$$

(3.4.-17)

$$F_2 = \tanh(\Phi_2^2)$$

(3.4.-18)

$$\Phi_2 = \max\left[2\frac{\sqrt{k}}{0.09\omega y}, \frac{500\mu}{\rho y^2 \omega}\right]$$

(3.4.-19)

where y is the distance to the closest surface.

The effective diffusivities for the SST $k-\omega$ model are given by:

$$\Gamma_k = \mu + \frac{\mu_t}{\sigma_k}$$

(3.4.-20)

$$\Gamma_\omega = \mu + \frac{\mu_t}{\sigma_\omega}$$

(3.4.-21)

where σ_k and σ_ω are the turbulent Prandtl numbers for k and ω, respectively. The difference between the standard (baseline) $k-\omega$ models is the method for the computation of the turbulent viscosity μ_t, which is computed by:

$$\mu_t = \frac{\rho k}{\omega}\frac{1}{\max[\frac{1}{\alpha^*}, \frac{SF_2}{a_1\omega}]}$$

(3.4.-22)

where S is the strain rate magnitude and α^* are given by:

$$S = \sqrt{2S_{ij}S_{ij}}$$

(3.4.-23)

where:

$$S_{ij} = \frac{1}{2}\left(\frac{\partial u_i}{\partial x_j} + \frac{\partial u_j}{\partial x_i}\right)$$

(3.4.-24)

Model constants:

$$\alpha = 0.5556\ \sigma_{k,1} = 1.176, \sigma_{\omega,1} = 2.0, \sigma_{k,2} = 1.0, \sigma_{\omega,2} = 1.168,\ a_1 = 0.31, \beta_{i,1} = 0.075, \beta_{i,2} = 0.0828,$$
$$\kappa = 0.41$$

(3.4.-25)

The given above model constants refer exclusively to SST $k-\omega$ model. Other constants are the same as for the standard (baseline) $k-\omega$ model.

3.5. Realizable k – ε Turbulence Model

The standard formulation of the $k-\varepsilon$ model is well-known and has been applied to many problems since it was developed by Launder and Spalding (1974). The transported variables are k, the turbulent kinetic energy, and specific dissipation ε, which determines the scale of turbulence.

The term “realizable” means that the model satisfies certain mathematical constraints of the Reynolds stresses, consistent with the physics of turbulent flows. According to the ANSYS Fluent User’s Guide the realizable version is preferred over the other models from $k-\varepsilon$ family. The model was used in a single simulation to compare it with the SST $k-\omega$, which was applied in every case presented in this work.

The modeled transport equations for k and ε in the realizable $k-\varepsilon$ model are:

$$\frac{\partial}{\partial t}(\rho k) = \frac{\partial}{\partial x_j}(\rho k u_j) = \frac{\partial}{\partial x_j}\left[\left(\mu + \frac{\mu_t}{\sigma_k}\right)\frac{\partial k}{\partial x_j}\right] + G_k + G_b - \rho\varepsilon - Y_M + S_k$$

(3.5.-1)

$$\frac{\partial}{\partial t}(\rho\varepsilon) = \frac{\partial}{\partial x_j}(\rho\varepsilon u_j) = \frac{\partial}{\partial x_j}\left[\left(\mu + \frac{\mu_t}{\sigma_\varepsilon}\right)\frac{\partial \varepsilon}{\partial x_j}\right] + \rho C_1 S\varepsilon - \rho C_2 \frac{\varepsilon^2}{k + \sqrt{\nu\varepsilon}} + C_{1\varepsilon}\frac{\varepsilon}{k}C_{3\varepsilon}G_b + S_\varepsilon$$

(3.5.-2)

where:

$$C_1 = max\left[0.43, \frac{\eta}{\eta + 5}\right] \tag{3.5.-3}$$

$$\eta = S\frac{k}{\varepsilon} \tag{3.5.-4}$$

$$S = \sqrt{2S_{ij}S_{ij}} \tag{3.5.-5}$$

In these equations, G_k represents the generation of turbulence kinetic energy. G_b is the generation of turbulence kinetic energy due to buoyancy, which is negligible for the combustor under investigation. Y_M represents the contribution of the fluctuating dilatation in compressible turbulence to the overall dissipation rate. C_1, C_2, $C_{1\varepsilon}$ and $C_{3\varepsilon}$ are constants. σ_k and σ_ε are the turbulent Prandtl numbers for k and ε, respectively. S_k and S_ε are user-defined source terms, which are set to zero in the present work.

As in other $k-\varepsilon$ models, the turbulent viscosity is computed from:

$$\mu_t = \rho C_\mu \frac{k^2}{\varepsilon} \tag{3.5.-6}$$

The difference between the realizable $k-\varepsilon$ model and the standard $k-\varepsilon$ model is that C_μ is no longer constant. It is computed from:

$$C_\mu = \frac{1}{A_0 + A_s\frac{kU^*}{\varepsilon}} \tag{3.5.-7}$$

where:

$$U^* \equiv \sqrt{S_{ij}S_{ij} + \tilde{\Omega}_{ij}\tilde{\Omega}_{ij}} \tag{3.5.-8}$$

and

$$\widetilde{\Omega}_{ij} = \Omega_{ij} - 2\varepsilon_{ijk}\omega_k \tag{3.5.-9}$$

$$\Omega_{ij} = \overline{\Omega_{ij}} - \varepsilon_{ijk}\omega_k \tag{3.5.-10}$$

where Ω_{ij} is the mean rate-of-rotation tensor, ε_{ijk} is the swapping tensor viewed in a moving reference frame with the angular velocity ω_k obtained from:

$$\widetilde{\Omega}_{ij} = \frac{1}{2}\left(\frac{\partial \tilde{u}_j}{\partial x_i} - \frac{\partial \tilde{u}_i}{\partial \delta}\right) \tag{3.5.-11}$$

The model constants A_0 and A_s are given by:

$$A_0 = 4.04 \tag{3.5.-12}$$

$$A_s = \sqrt{6}cos\phi \tag{3.5.-13}$$

where

$$\phi = \frac{1}{3}cos^{-1}\left(\sqrt{6}W\right) \tag{3.5.-14}$$

$$W = \frac{S_{ij}S_{jk}S_{ki}}{\tilde{S}^3} \tag{3.5.-15}$$

$$\tilde{S} = \sqrt{S_{ij}S_{ij}} \tag{3.5.-16}$$

S_{ij} represents the rate of deformation of the average velocity field calculated by:

$$S_{ij} = \frac{1}{2}\left(\frac{\partial u_j}{\partial x_i} + \frac{\partial u_i}{\partial x_j}\right) \tag{3.5.-17}$$

The model constants C_2, σ_k and σ_ε were established to ensure that the model performs well for certain canonical flows. The model constants are:

$$C_{1\varepsilon} = 1.44, C_2 = 1.9, \sigma_k = 1.0, \sigma_\varepsilon = 1.2$$

3.6. Eddy Dissipation Concept (EDC) Combustion Model

The Eddy Dissipation Concept model was developed by Magnussen (1981). It is an extension of the Eddy Dissipation Model (EDM) that allows inclusion of detailed chemical mechanisms in turbulent flows. It assumes that reactions occur within small turbulent structures, called the fine scales, where all the turbulent kinetic energy is dissipated into heat. The volume fraction of the fine scales is modeled as:

$$\xi^* = C_\xi \left(\frac{\nu\varepsilon}{k^2}\right)^{1/4} \tag{3.6.-1}$$

where $*$ denotes fine-scale quantities, $C_\xi = 2.1377$, ν is the kinematic viscosity.

Species are assumed to react in the fine structures over a time scale:

$$\tau^* = C_\tau \left(\frac{\nu}{\varepsilon}\right)^{1/2} \tag{3.6.-2}$$

Where C_τ is a time scale constant and $C_\tau = 0.4082$.

The following expression has been developed (Magnussen 1989) to model the rate of mass flow rate between the fine scales and its surroundings:

$$m = \frac{\xi^2}{\tau} \tag{3.6.-3}$$

The rate of mass transfer of each species to the region of the fine scales is defined by:

$$m_i = m(Y_i^* - Y_i^0) \tag{3.6.-4}$$

Where Y_i^* and Y_i^0 are the mass fraction of the species i in the fine scales region and in the surrounding region, respectively.

The production rate of each species can be defined by the following equation:

$$\dot{\omega}_i = \frac{\xi^3 \bar{\rho}}{\tau} \frac{\left(Y_i^* - \tilde{Y}_i\right)}{1 - \xi^3} \tag{3.6.-5}$$

where the mean mass fraction of species $\tilde{Y}_i$ is defined by the following:

$$\tilde{Y}_i = \xi^3 Y_i^* + (1 - \xi^3) Y_i^0 \tag{3.6.-6}$$

Assuming the small turbulent structures are small reactors at constant pressure, the mass fractions of chemical species in the fine structures are obtained from the integration between $t = 0$ and $t = \tau$ of the formation/destruction rate of each chemical species:

$$\frac{d}{dt}\left(\rho Y_i(t)\right) = \dot{\omega}_i \tag{3.6.-7}$$

where $\dot{\omega}_i$ represents the formation/destruction rate of chemical species given by the following expression:

$$\dot{\omega}_i = M_i \sum_r^{N_r} R_{i,r} \tag{3.6.-8}$$

Before solving the species transport equation, equation (3.6.-7) is solved for all control volumes at each iteration of the calculation algorithm. Species transport equation is given by the following expression (assuming, that the mass diffusion flux is given by Fick's law):

$$\frac{\partial(\bar{\rho}\tilde{y}_i)}{\partial t} + \frac{\partial(\bar{\rho}\tilde{u}_j\tilde{y}_i)}{\partial x_j} = \frac{\partial}{\partial x_j}\left[\overline{\rho D_i^M \frac{\partial y_i}{\partial x_j}} - \bar{\rho}\widetilde{u_j'' y_i''}\right] + \dot{\omega}_i \tag{3.6.-9}$$

In the solution of equation (3.6.-7), the mean values of temperature and mass fraction of species in each computational cell, are used to define the initial conditions. The mass fraction of species in the fine structures Y_i^* is obtained from the integration of the equation (3.6.-7). With these values the source terms of the chemical species transport equation are calculated by equation (3.6.-5). The chemical species mass fraction $\tilde{Y}_i$ are obtained from equation (3.6.-9).

The temperature is iteratively determined from the enthalpy according to the following equation:

$$\tilde{h} = \sum_i^n \tilde{Y}_i h_i(\tilde{T})$$

(3.6.-10)

The mean density is calculated from the ideal gas law:

$$\frac{1}{\bar{\rho}} = \frac{R\tilde{T}}{p} \sum_i^n \frac{\tilde{Y}_i}{M_i}$$

(3.6.-11)

3.7. DRM-19 Reaction Mechanism

The EDC model described above was coupled with a detailed chemical mechanism called DRM-19, which is the reduced reaction set based on GRI 1.2 (Frenklach et al. 1995). The mechanism applies to the methane-air mixtures, which is the case of the present study. It was developed by truncation of the original set with the objective of developing the smallest set of reactions that is able to reproduce closely the main combustion characteristics predicted by the full mechanism (Kazakov and Frenklach).

The choice of the reduced over full mechanism was dictated by the limited computational resources. The comparison of the two, DRM-19 and GRI 1.2 mechanisms, is presented in chapter 5. The mechanism contains 21 species, namely: H_2, H, O, O_2, OH, H_2O, HO_2, CH_2, $CH_2(S)$, CH_3, CH_4, CO, CO_2, HCO, CH_2O, CH_3O, C_2H_4, C_2H_5, C_2H_6, N_2, Ar. It involves 84 reactions. It has been designed for the initial conditions (conditions under which the reaction occurs) specified in Table 3.1 and for adiabatic flames at pressures 1 atm and 20 atm.

Table 3.1 Initial design conditions for the DRM-19 mechanism (Kazakov and Frenklach).

Parameter	Range	Unit
Pressure	0.1 - 50	atm
Temperature	1300 - 2500	K
Excess air coefficient	0.5 - 5	-

3.8. Discrete Ordinates (DO) Radiation Model

Radiative heat transfer accounts for a significant part of the transferred heat due to high temperatures related to the combustion process. In the present study, the Discrete Ordinates model was applied. The DO model spans the entire range of absorption thicknesses and allows to solve problems of radiation in combustion problems. The radiative transfer equation (RTE) for an absorbing, emitting and scattering medium at position $\vec{r}$ in the direction $\vec{s}$ is given by:

$$\frac{dI(\vec{r},\vec{s})}{ds} + (a+\sigma_s)I(\vec{r},\vec{s}) = an^2\frac{\sigma T^4}{\pi} + \frac{\sigma_s}{4\pi}\int_0^{4\pi} I(\vec{r},\vec{s}')\phi(\vec{s},\vec{s}')d\Omega'$$

(3.8.-1)

where: $\vec{r}$ – position vector, $\vec{s}$ – direction vector, $\vec{s}'$ - scattering direction vector, s – path length, a – absorption coefficient, n – refractive index, σ_s – scattering coefficient, σ – Stefan-Boltzmann constant, I – radiation intensity (depends on $\vec{r}$ and $\vec{s}$), T – local temperature, ϕ – phase function, Ω' - solid angle.

The DO radiation model requires the absorption coefficient as an input. ANSYS Fluent provides the weighted-sum-of-gray-gases model (WSGGM) for computation of a variable absorption coefficient. This approach has been chosen in all performed simulations. The basic assumption of the WSGGM is that the total emissivity over the distance can be presented as:

$$\varepsilon = \sum_{i=0}^{I} a_{\varepsilon,i}(T)(1 - e^{-\kappa_i p s})$$

(3.8.-2)

where $a_{\varepsilon,i}$ is the emissivity weighting factor for i – th fictitious grey gas, the bracketed quantity is the i – th fictitious grey gas emissivity, κ_i is the absorption coefficient of the i – th grey gas, p is the sum of the partial pressures of all absorbing gases and s is the path length. Values of $a_{\varepsilon,i}$ and κ_i are set by ANSYS Fluent and were obtained from Coppalle and Vervisch (1983) and Smith et al. (1982). The DO model considers the radiative transfer equation (RTE) in the direction $\vec{s}$ as a field equation. The equation (3.6.-1) is given by:

$$\nabla\cdot(I(\vec{r},\vec{s})\vec{s}) + (a+\sigma_s)I(\vec{r},\vec{s}) = an^2\frac{\sigma T^4}{\pi} + \frac{\sigma_s}{4\pi}\int_0^{4\pi} I(\vec{r},\vec{s}')\phi(\vec{s}\cdot\vec{s}')d\Omega'$$

(3.8.-3)

The source term of the energy conservation equation related to heat exchange by radiation is calculated by the following expression:

$$q_R''' = \kappa_i(4\sigma T^4 - G_{inc})$$

(3.8.-4)

where T is temperature of the medium and G_{inc} is the incident radiation calculated by:

$$G_{inc} = \int_{4\pi} I d\Omega$$

(3.8.-5)

Chapter 4

Numerical Simulation

4.1. Numerical Details

As it was mentioned before, the commercial code ANSYS Fluent v17.1 was used for the simulation of the reactive flow inside the combustion chamber. The solution method for all the simulations was the pressure-based steady-state segregated algorithm SIMPLEC. The equations involved in the simulations were: Energy, Viscous (SST $k-omega$), Radiation (Discrete Ordinates (DO)) and Species (Species Transport, Reactions). In order to reduce the computational cost of chemistry calculations, the In-Situ Adaptive Tabulation (ISAT) algorithm or Pope (1997) was used. The ISAT tolerance was set equal to 10^{-4}. The computational grid is described in part 4.2. Boundary conditions and material properties are described in parts 4.4 and 4.5.

When it comes to the setup of the models, which were used in the simulations, all the settings were left default with the exception of Discrete Ordinates (DO) model, where the Angular Discretization was specified as presented in Table 4.2 in order to achieve more reliable results concerning radiation.

Table 4.1 Angular discretization setup in Discrete Ordinates (DO) model.

Parameter	Value
Theta Divisions	4
Phi Divisions	4
Theta Pixels	3
Phi Pixels	3

Theta Divisions (N_θ) and *Phi Divisions* (N_ϕ) define the number of control angles used to discretize each octant of the angular space, which is presented in figure 4.1.

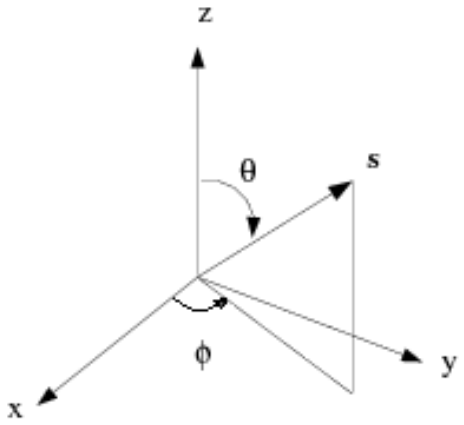

Fig. 4.1 Angular coordinate system (ANSYS Theory Guide 2016).

Theta Pixels and *Phi Pixels* are used to control the pixelation that accounts for any control volume overhang. For problems involving symmetry, periodic, specular, or semi-transparent boundaries, a pixelation of at least 3 x 3 is recommended to achieve acceptable results. The pixelation of control volume is presented in figure 4.2.

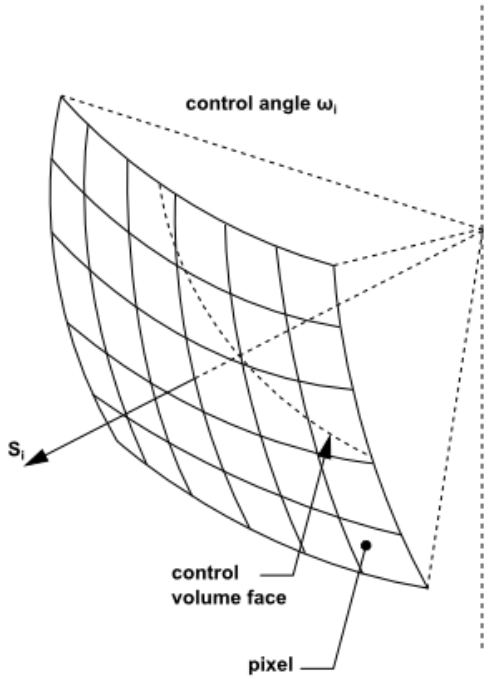

Fig. 4.2 Pixelation of the control volume (ANSYS Theory Guide 2016).

The solution options and spatial discretization schemes chosen for each solved equation are listed in table 4.2

Table 4.2 Solution and discretization methods.

Gradient	Least Squares Cell Based
Pressure	PRESTO!
Momentum	Second Order Upwind
Turbulent kinetic energy	Second Order Upwind
Turbulent dissipation rate	Second Order Upwind
Energy	Second Order Upwind
Species	Second Order Upwind
Discrete ordinates	Second Order Upwind

The convergence of the solution was verified by all the simulations based on the sum of the residuals for each equation and based on the behavior of the pre-set monitoring points. The convergence criterion demanded the residuals to they fall below the values listed in table 4.3.

Table 4.3 Criterion of convergence for the sum of residuals.

Equation	Residuals
Continuity	10^{-5}
X - velocity	10^{-5}
Y - velocity	10^{-5}
Z - velocity	10^{-5}
Energy	10^{-5}
Turbulent kinetic energy, k	10^{-5}
Specific dissipation rate, omega	10^{-5}
DO - intensity	10^{-5}
Species	10^{-5}

The other criterion was based on the behavior of two kinds of monitors. One monitor was a point where the temperature was measured. It was located 40 mm from the central axis and 181 mm away from the burner. The second monitor was *Area-Weighted Average*, which measured the molar fraction of CO_2 on the outlet of the combustor. The desired behavior of monitors was to remain stable in relation to the number of iterations.

The use of EDC model requires a specific approach to performing the simulation. For the combustion process to begin, it is often necessary to initialize it, for instance by adding a high temperature region as a boundary condition at the beginning of the simulation. The other method, which was applied in this study, is to begin the simulation with the Non-Premixed Combustion (NPC) model and then switch to the EDC model (artificial source of ignition was not necessary in this case). The procedure applied for all the simulations is presented in figure 4.3.

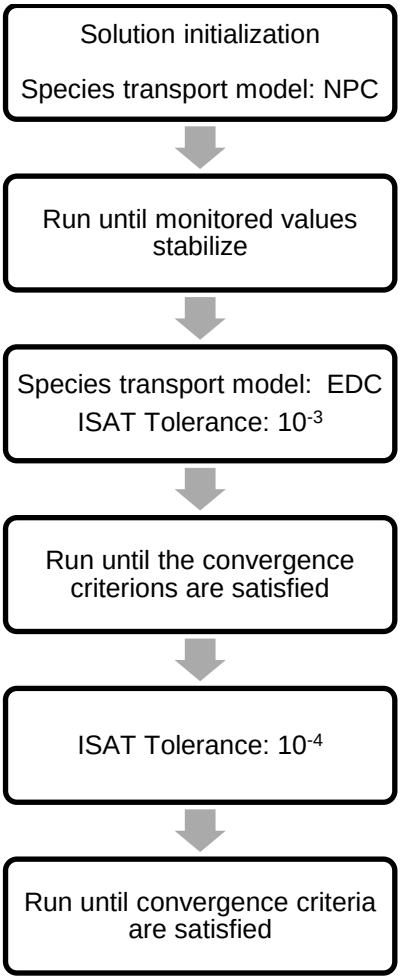

Fig. 4.3 Simulation procedure.

4.2. Computational Domain

Details concerning the construction of the combustor on which the experiments were conducted are described in chapter 2. The simulation involves the processes regarding the combustion phenomena, which take place within the combustion chamber. The computational domain represents the interior of the combustor, in other words, the computational domain is a representation of volume filled in with the gas mixture.

Due to the symmetrical design of the combustor and the symmetrical nature of the flow, the simulation can be performed for 1/16 ($22{,}5^{o}$) of the combustion chamber. The simulation of the whole combustion chamber would require far more computational time and would produce the same result, as can be achieved with the geometry representing 1/16 of the actual object. The inlet ducts were included in the geometry in order to develop the flow before the reactant gasses reach the combustion chamber. In chapter 5.3 (p. 61) the validity of such approach will be verified. It may be possible, that setting the boundary condition at the plane representing the inlet area, where the reactants reach the tube of the combustor, produces the same or negligibly different results as compared to the simulation involving the inlet ducts.

Figure 4.4 presents the geometry of the combustor (configuration A) which was modeled for the purpose of the given study.

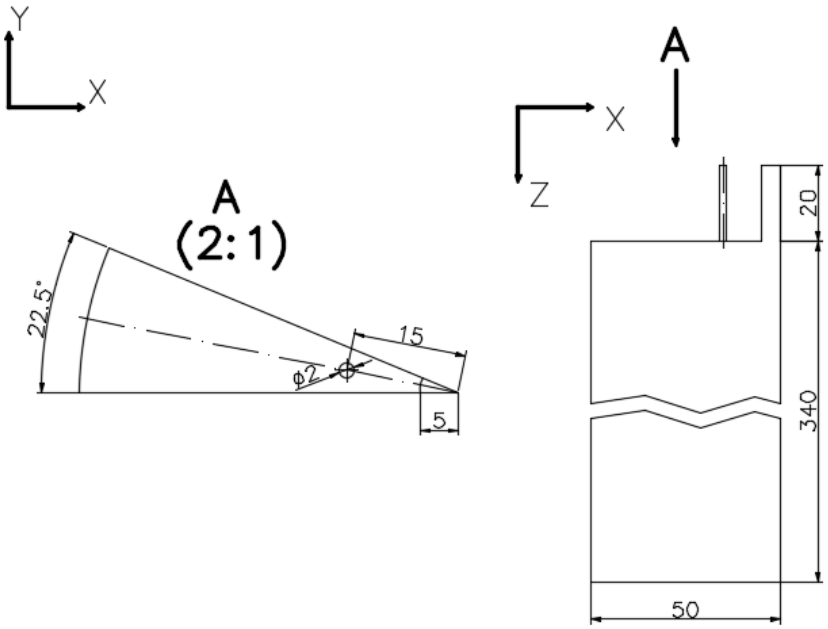

Fig. 4.4 The geometry of the combustion chamber used in the numerical simulation.

Figure 4.5 shows the screens from ANSYS Workbench component, which present the modeled geometry in different views.

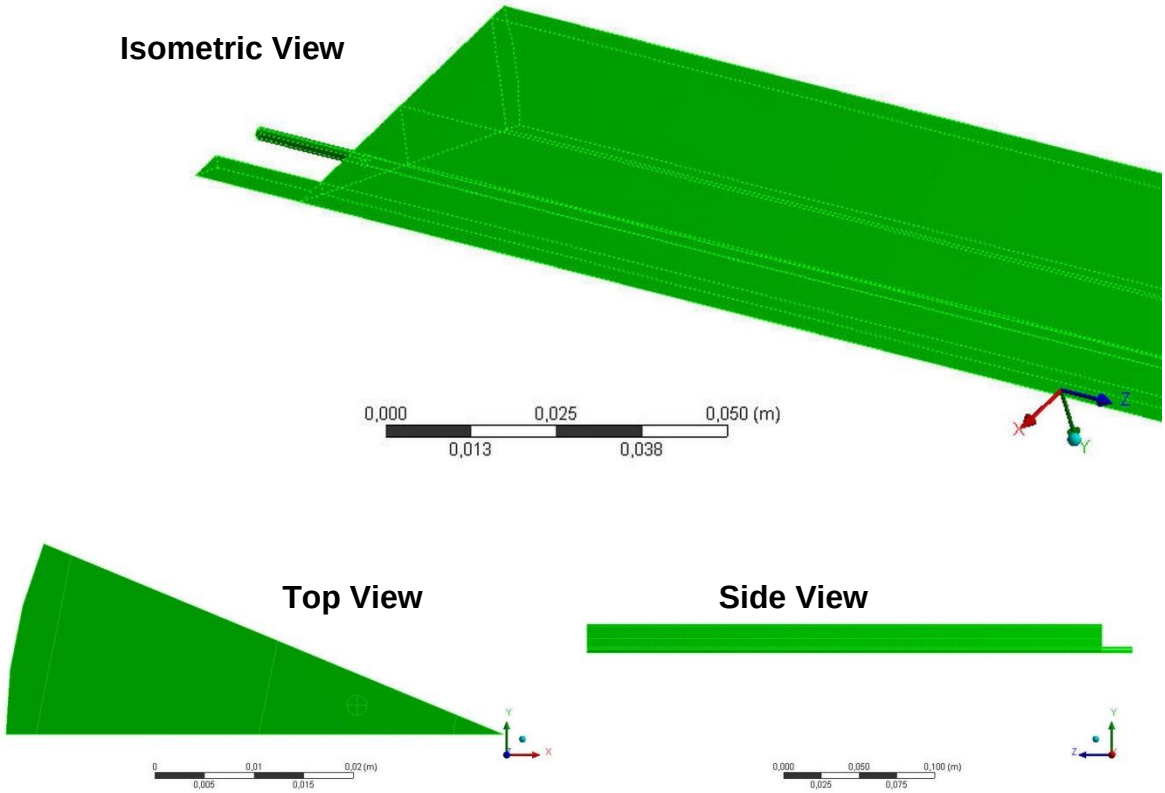

Fig. 4.5 Screenshots of geometry generated in ANSYS Workbench.

4.3. Computational Grid

In order to determine the number of mesh cells, which is required to produce satisfactory results for the given problem, three unstructured meshes were created in ANSYS Workbench for the geometry as in configuration A (air inlet diameter of 10 mm and the fuel inlet distance of 15 mm):

- Coarse with approximately 40 000 cells
- Medium with approximately 136 000 cells
- Fine with approximately 352 000 cells

The grid independence study of these three meshes is described in chapter 5. The purpose of this analysis is to find the optimal mesh refinement. The more elements used, the more computational time it takes to perform the calculations with different burner configurations. Therefore determination of the optimal mesh refinement makes it possible to perform calculations for various cases, which is one of the basic requirements of this work. Furthermore, it is generally considered a good engineering practice to always seek for the simplest, yet accurate model.

The three meshes are presented in figures 4.6-4.8.

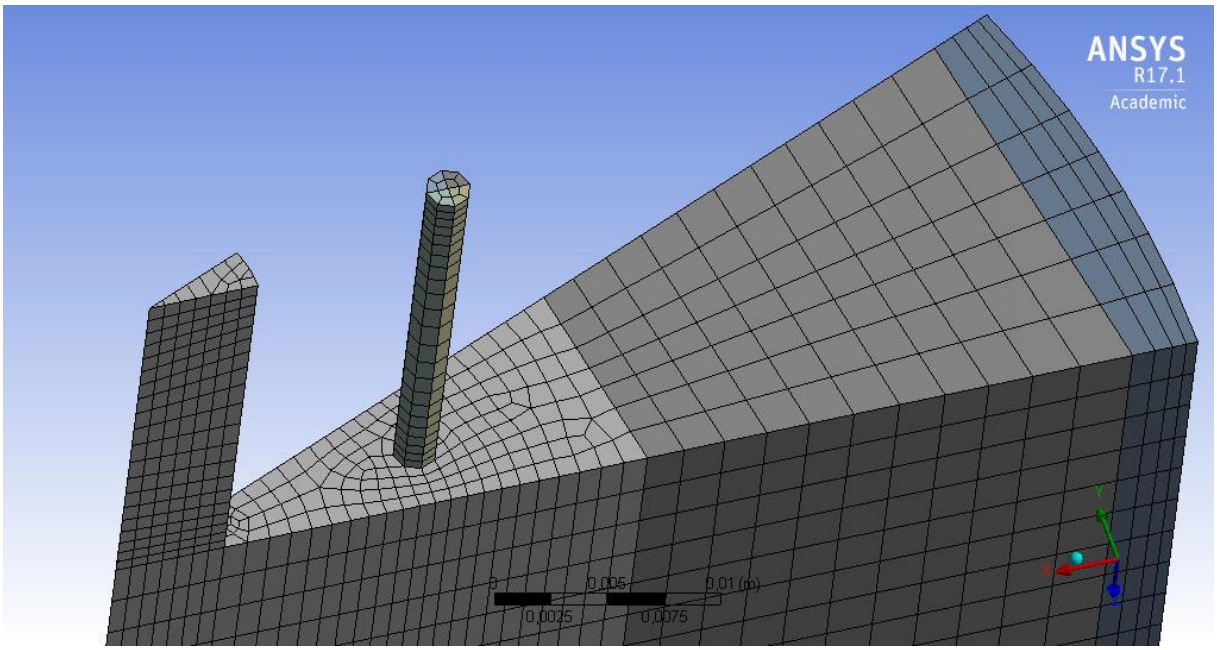

Fig. 4.6 Coarse mesh with ~ 40 000 cells, configuration A.

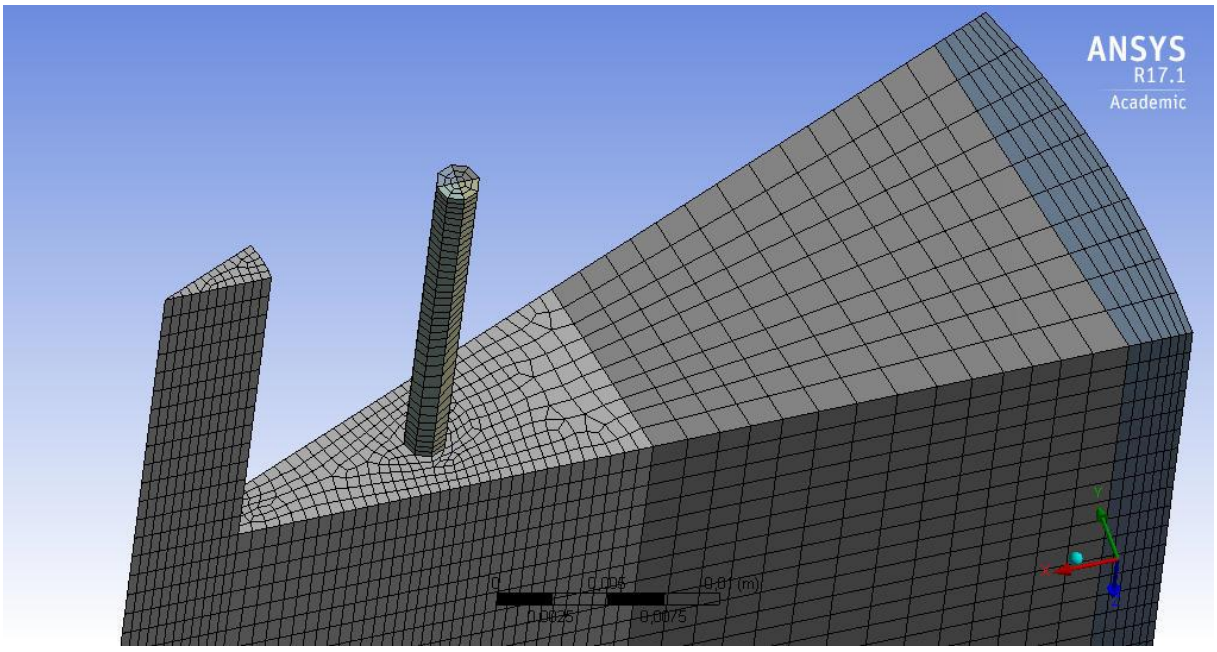

Fig. 4.7 Medium mesh with ~ 136 000 cells, configuration A.

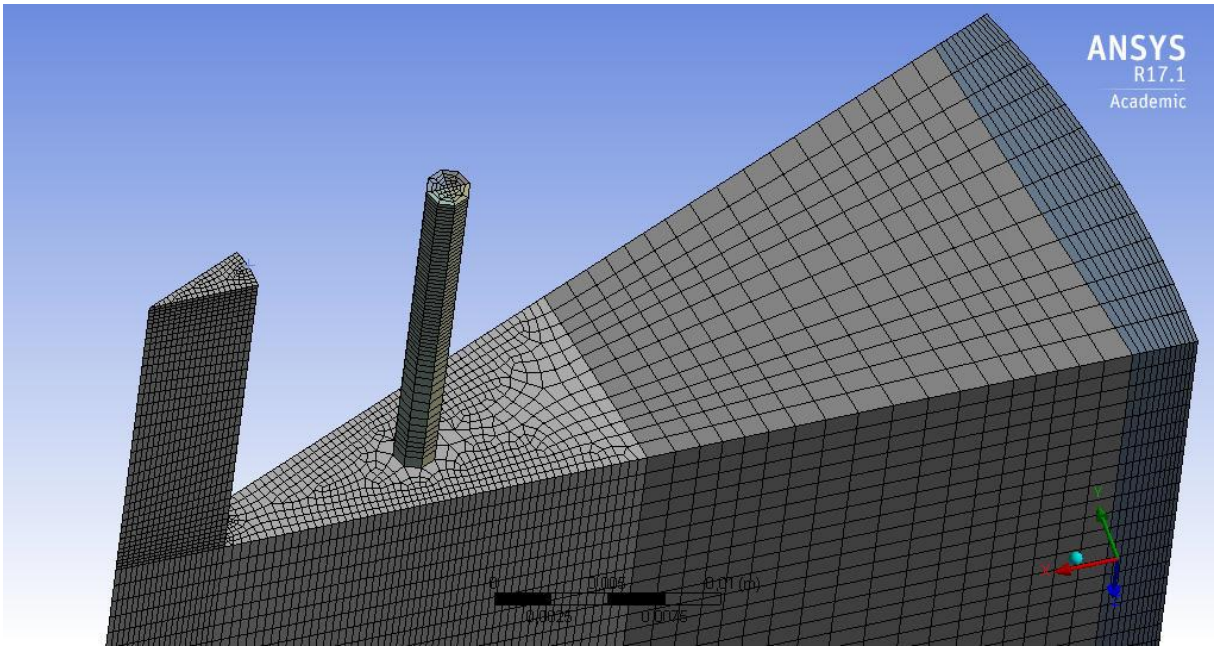

Fig. 4.8 Fine mesh with ~ 352 000 cells, configuration A.

As it can be seen in the figures, the geometry was sliced into parts, which were meshed with different cell sizes. Such approach was implemented in order to provide finer meshing in the main region of the reaction zone, where higher gradients of temperature and velocity are expected (based on the results of the past studies of Veríssimo et al. (2011)). The result of such solution aims to reduce the number of elements in regions, where fine meshing is not necessary whilst providing more elements where the variations are more intense. In the given simulation it was expected that the main reaction zone would be in the central area of the combustion chamber, along and around the axis of the combustor and in the vicinity of the burner.

Apart from the central zone of the combustion chamber, the mesh was refined in the region near the side wall of the combustor chamber in order to improve the accuracy of the heat transfer simulation between the side wall of the combustor and the medium within the combustor.

While building the mesh, its quality has been assessed with the regard to the parameter “Skewness”, which is based on the geometrical orientation of the mesh. It measures how much the generated mesh differs from ideal orthogonal mesh cell. In this case, as it can be seen in the above figures, the mesh is hexahedral. Therefore, skewness for such case is the measure of how much the given cells differs from the ideal cell, which for the hexahedral mesh is a cube. The figure 4.10 illustrates the difference between ideal and highly skewed quad cell.

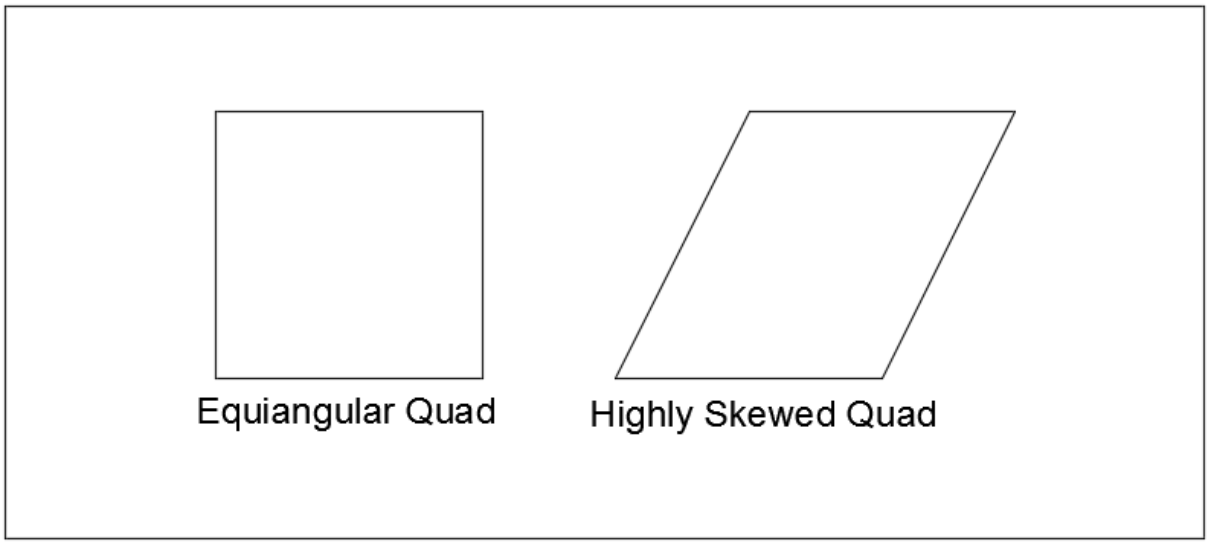

Fig. 4.9 Illustration of equiangular and highly skewed quad cell.

Skewness parameter ranges from 0 to 1, where values close to 0 indicate better quality of a given mesh.

Highly skewed faces and cells are not acceptable because the equations are solved with the assumption that the cells are relatively equilateral/equiangular.

In the given case, the skewness is defined as:

$$max\left[\frac{\theta max - \theta_e}{180 - \theta_e}, \frac{\theta_e - \theta_{min}}{\theta_e}\right] \quad (4.3.\text{-}1)$$

where θmax is the largest angle in the face or cell, θ_{min} is the smallest angle in the face or cell and θ_e is an angle for an equiangular face/cell (e.g., 60 for a triangle, 90 for a square).

According to the ANSYS User's Guide, the skewness should be evaluated according to the guidelines presented in table 4.4.

Table 4.4 Guidelines for interpretation of different values of skewness parameter.

Value of Skewness	Cell Quality
1	degenerate
0.9 — <1	bad (sliver)
0.75 — 0.9	poor
0.5 — 0.75	fair
0.25 — 0.5	good
>0 — 0.25	excellent
0	equilateral

During the process of mesh design, the value of average skewness should was kept below 0.25, which indicates the excellent quality of mesh cells. The values of average skewness for generated meshes are presented in table 4.5.

Table 4.5 Average skewness values for the designed meshes.

Parameter	Coarse mesh	Medium mesh	Fine mesh
Skewness	0.138	0.130	0.121

In order to perform the sensitivity analysis, the simulations have been performed for the set of conditions described in tables 2.1 and 2.2 for configuration A. The purpose of such analysis was to find out whether there is a correlation between the results and the number of mesh cells and to see how the simulation manages to represent the measurements obtained during the experiment.

All the simulations for the modified burner configurations were designed with a similar mesh structure and a similar number of cells as the one chosen as a result of the grid independence study presented in chapter 5.

4.4. Tested Configurations and Test Conditions

The main purpose of this study is to investigate numerically the impact of different burner configurations on the combustion process within the combustor. For this purpose, different configurations were designed. In order to organize the simulation, the different configurations were assigned names as listed in table 4.6.

Table 4.6 Simulated burner configurations.

Configuration	Air inlet diameter D_{air} (mm)	Air fuel inlets distance L (mm)
A (available detailed experimental data)	10	15
B	9	15
C	8	15
D	7	15
E	6	15
F	10	7.5
G	8	7.5
H	6	7.5
I	10	30
J	8	30
K	6	30

The grid independence study was performed for configuration A, for which three different meshes were used. Grid independence study was conducted on the basis of the cell number. All the details concerning the grid are described in part 4.3.

Test conditions are presented in table 4.7. As it was mentioned before, changing the inlet air diameter while maintaining the constant excess air coefficient induces the changes of the velocity at the air inlet for constant power level.

Table 4.7 Test conditions.

Parameter	Value
Input power	10 kW
Excess air coefficient	1,3
Air inlet temperature	673 K
Air inlet velocity	Configurations: A, F, I – 108.47 m/s B – 133.92 m/s C, G, J – 169.49 m/s D – 221.37 m/s E, H, K – 301.31 m/s

Air inlet diameter	Configurations: A, F, I - 10 mm B - 9 mm C, G, J - 8 mm D - 7 mm E, H, K - 6 mm
Air inlet species (mole fraction)	0.21 O_2 0.79 N_2
Air inlet turbulence specification	Turbulent intensity - 5 % Hydraulic diameter = Air inlet diameter
Fuel inlet temperature	298 K
Fuel inlet velocity	6.06 m/s
Fuel inlet diameter	2 mm
Fuel inlet species (mole fraction)	1 CH_4
Fuel inlet turbulence specification	Turbulent intensity - 5 % Hydraulic diameter = Fuel inlet diameter
Outlet pressure	1 atm
Side wall temperature	1421 K
Front wall temperature	1204 K
Inlet ducts wall temperature (*fuel_inlet_wall*, *air_inlet_side_wall*)	1204 K
Wall emissivity (all walls)	0.85

Temperature boundary conditions at the walls were approximated on the basis of the gas temperatures obtained in the experimental study with configuration A. These temperatures were measured in points presented in chapter 2. The temperature was linearly extrapolated taking into account the average temperatures of gas measured parallel to the wall as shown in figure 4.7. T_{avg_05} and T_{avg_10} for the approximation of side wall temperature. T_{avg_11} and T_{avg_45} for front wall and duct walls temperatures.

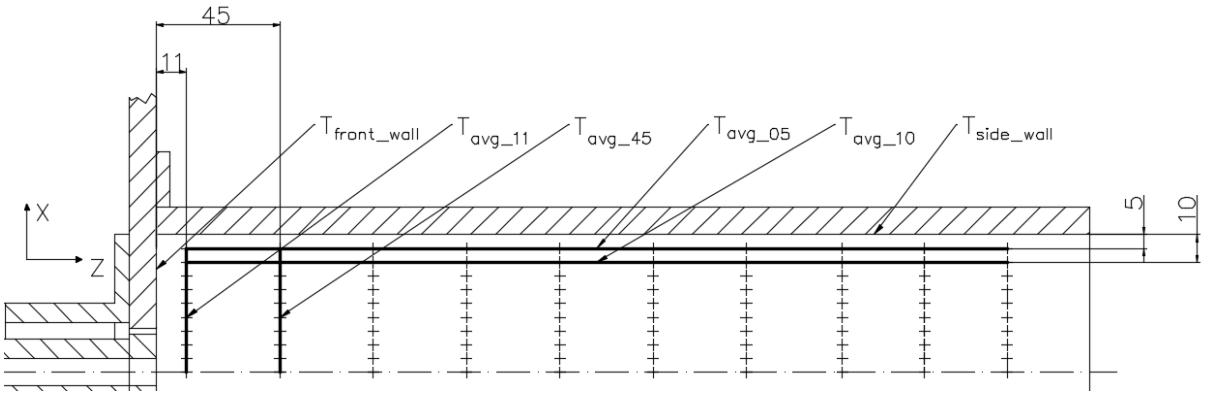

Fig. 4.10 Average gas temperatures used for the linear approximation of wall temperatures.

Such approach was applied, because the wall temperatures were not measured experimentally. The approximation is shown on the graphs in figures 4.11 and 4.12.

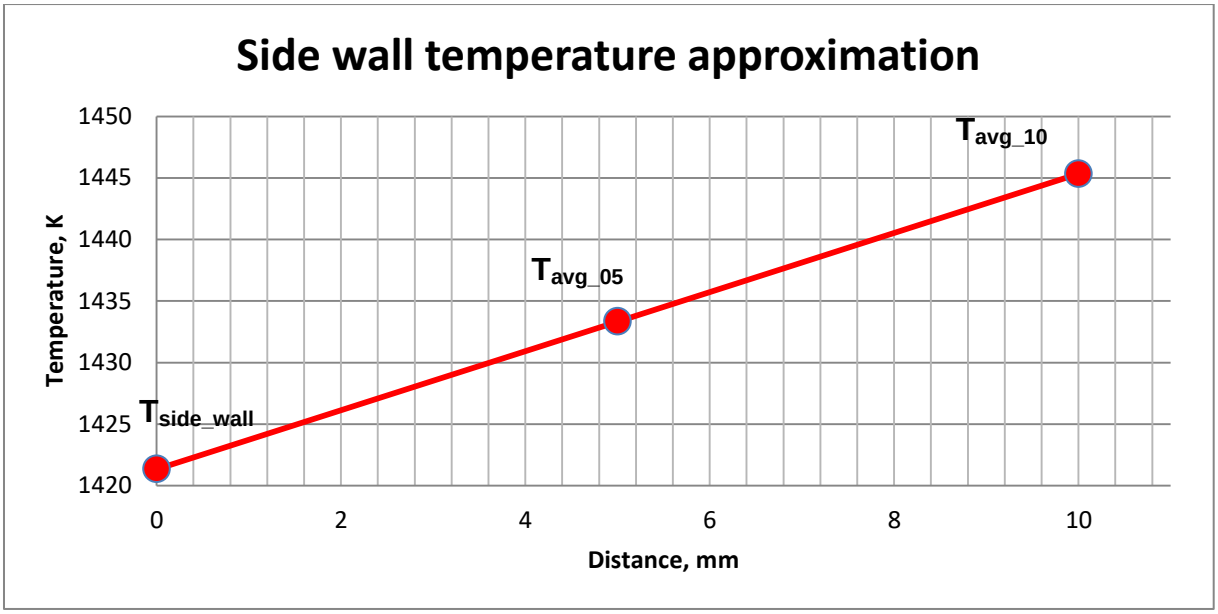

Fig. 4.11 Side wall temperature approximation.

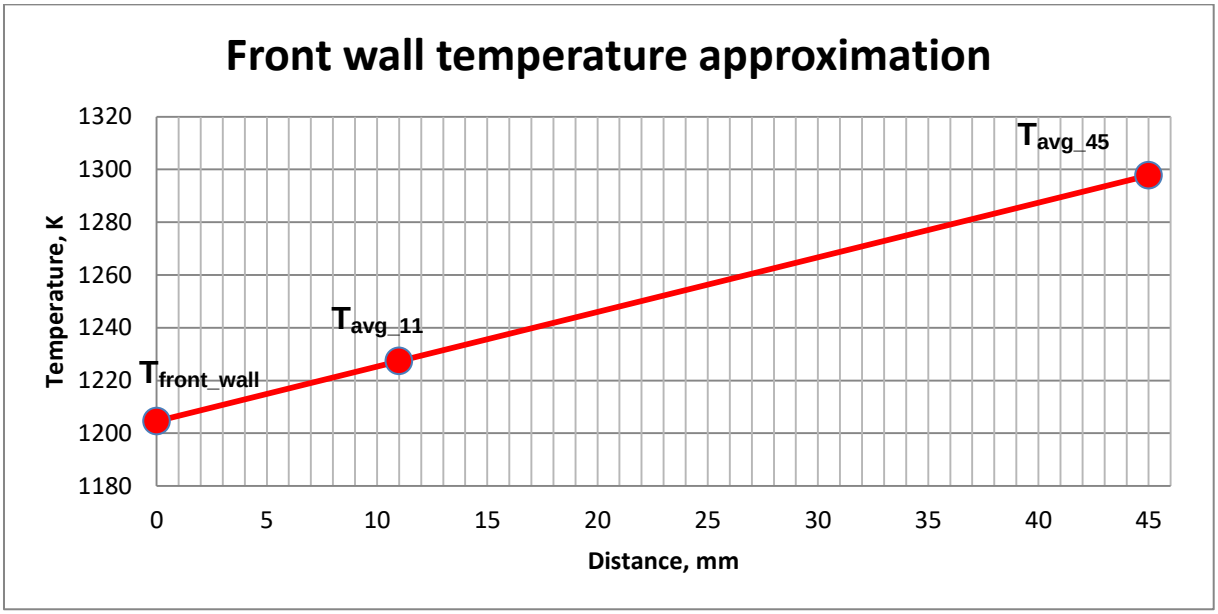

Fig. 4.12 Front wall temperature approximation.

Symmetry boundary condition could be applied in the given case because it was experimentally observed, that the flow is axisymmetrical (Veríssimo et al. 2015).

4.5. Mixture Properties

In this section, the properties of the gas mixture are presented. The chemical species are taken from the DRM-19 mechanism. The mixture properties originate from the thermodynamic database of DRM-19 mechanism and from Fluent database with the exception of the absorption coefficient, which was specified as *wssgm-domain-based*.

The *wssgm-domain-based* setting means that the mean beam length approach is used for the calculation of the absorption coefficient and Fluent will compute the mean beam length based on an average dimension of the domain. Mean beam length represents the average contributions of different beam lengths from the gas body to the striking surface.

The properties are presented in table 4.8.

Table 4.8 Material properties of the DRM-19 mixture.

Mixture species	Ar, N_2, C_2H_6, C_2H_5, C_2H_4, CH_3O, CH_2O, HCO, CO_2, CH_4, CH_3, CH_2<S>, CH_2, HO_2, H_2O, OH, O_2, O, H, H_2
Reaction	finite-rate
Mechanism	reaction-mechs
Density	incompressible-ideal-gas
Specific Heat Cp	mixing-law
Thermal Conductivity	0.0454 W/mK
Dynamic viscosity	1.72×10^{-5} kg/ms
Mass Diffusivity	2.88×10^{-5} m^2/s
Absorption Coefficient	wsggm-domain-based
Scattering Coefficient	0 [1/m]
Refractive Index	1

Chapter 5

Results and Discussion

5.1. Introduction

In this chapter, the simulation results are presented and discussed.

First of all the grid independence study is presented, which was conducted in order to determine the optimal number of mesh cells required for further simulations.

Subsequently, the influence of the geometry (configuration A) with and without ducts, the influence of turbulence model SST $k-\omega$ and Realizable $k-\varepsilon$, the influence of DRM-19 and GRI 1.2 chemical mechanisms on the solution are tested.

In the last part, the results of all the simulations with different burner configurations are presented with the objective to find out what is the influence of these modifications on the combustion process with reference to FLOX combustion regime described in chapter 1.

5.2. Grid Independence Study

This part contains the study on the influence of mesh granularity (number of cells) on the results. The predictions obtained in the simulations performed on the three meshes described in part 4.3 (coarse, medium, fine) are compared with the experimental data. The comparison involves axial mean temperature profiles and concentrations of species CO_2, CO and O_2. The profiles are presented in figure 5.1.

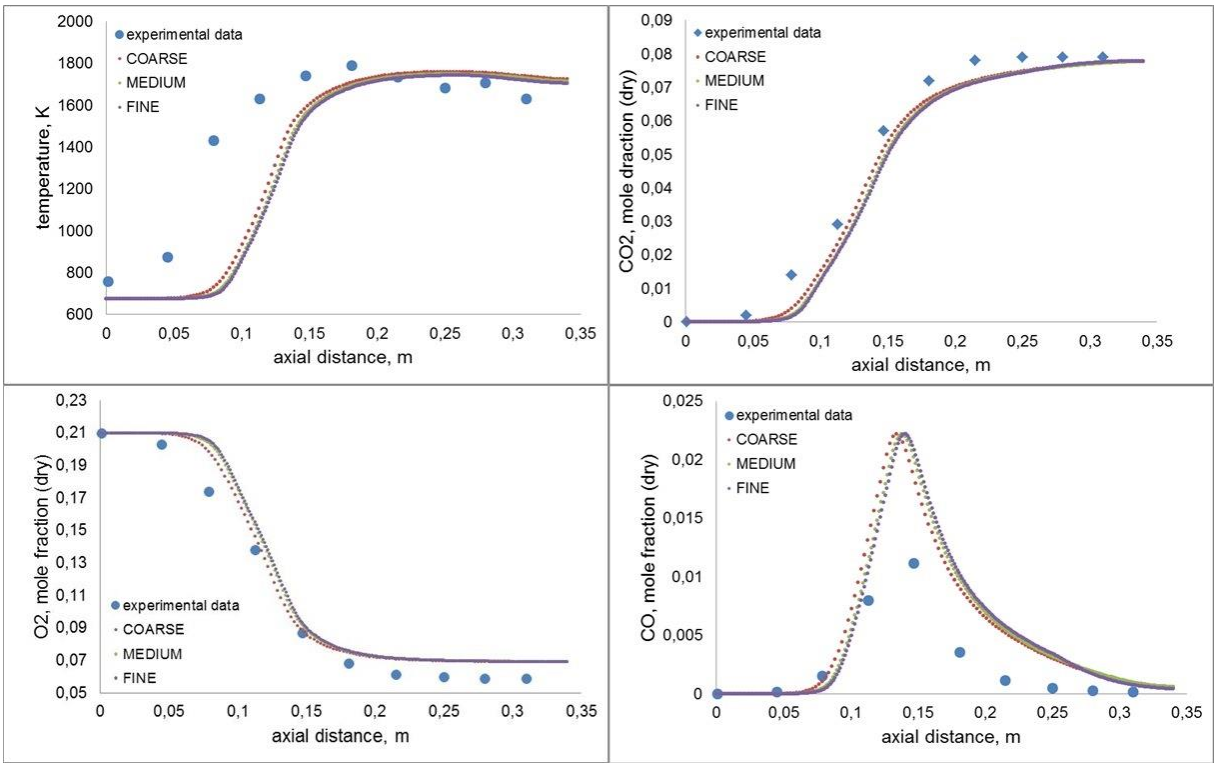

Fig. 5.1 Predicted and measured axial profiles of mean temperature, CO2, O2 and CO mean molar fractions on a dry basis.

As it can be observed the coarse mesh, with approximately 40 000 elements is sufficient to produce very close predictions when comparing to the other meshes containing more elements. The another conclusion, which can be made on the basis of this analysis is, that disregard of the mesh refinement, all the model's predictions are in fair agreement with the experimental data. These conclusions are the foundation for the choice of the reasonable number of cells for the models with modified geometry and are a good indicator of the validity of predictions produced by the models which represent cases for which the experimental data are not available.

5.3. Geometry Influence

The simulations have been performed with geometries that include inlet ducts for air and fuel of 20 mm length in order to improve the shape of the velocity profile at the entrance to the combustor. It should be noted, that in the given case, adding the ducts increases the computational domain by a small fraction and thus the computational time is practically the same. The difference between the two geometries is presented in figure 5.2.

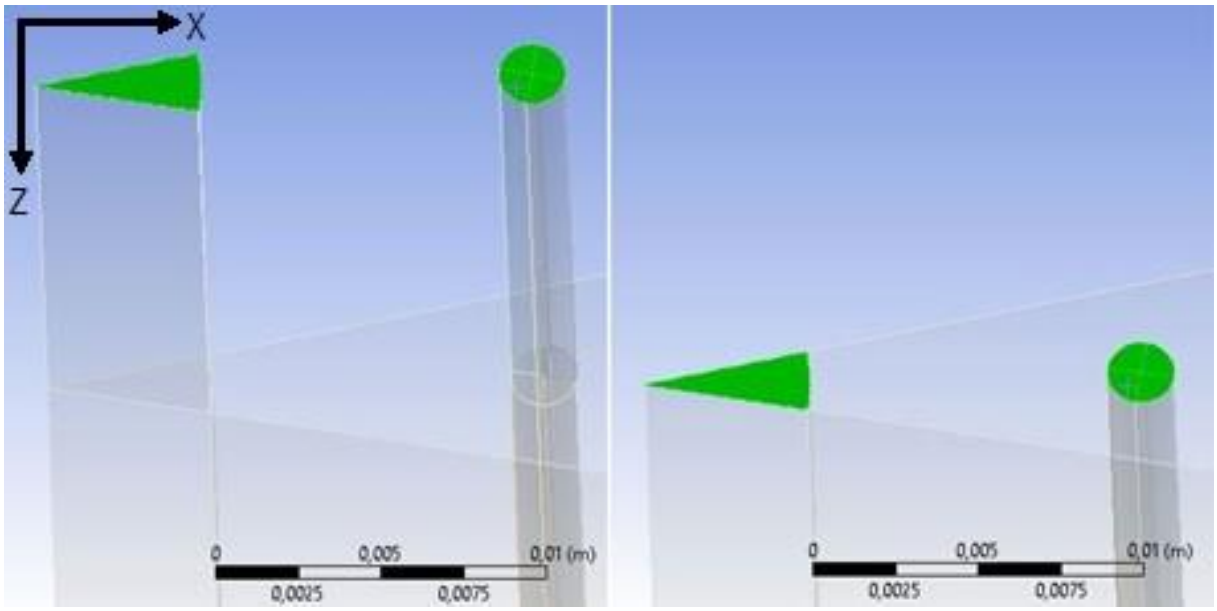

Fig. 5.2 Geometries with and without inlet ducts (configuration A).

This part aims to determine what is the influence of removing inlet ducts from the geometry on the predictions of axial temperature, velocity, CO_2, O_2 and CO species concentrations profiles. The tests were performed in configuration A and are compared with available experimental data.

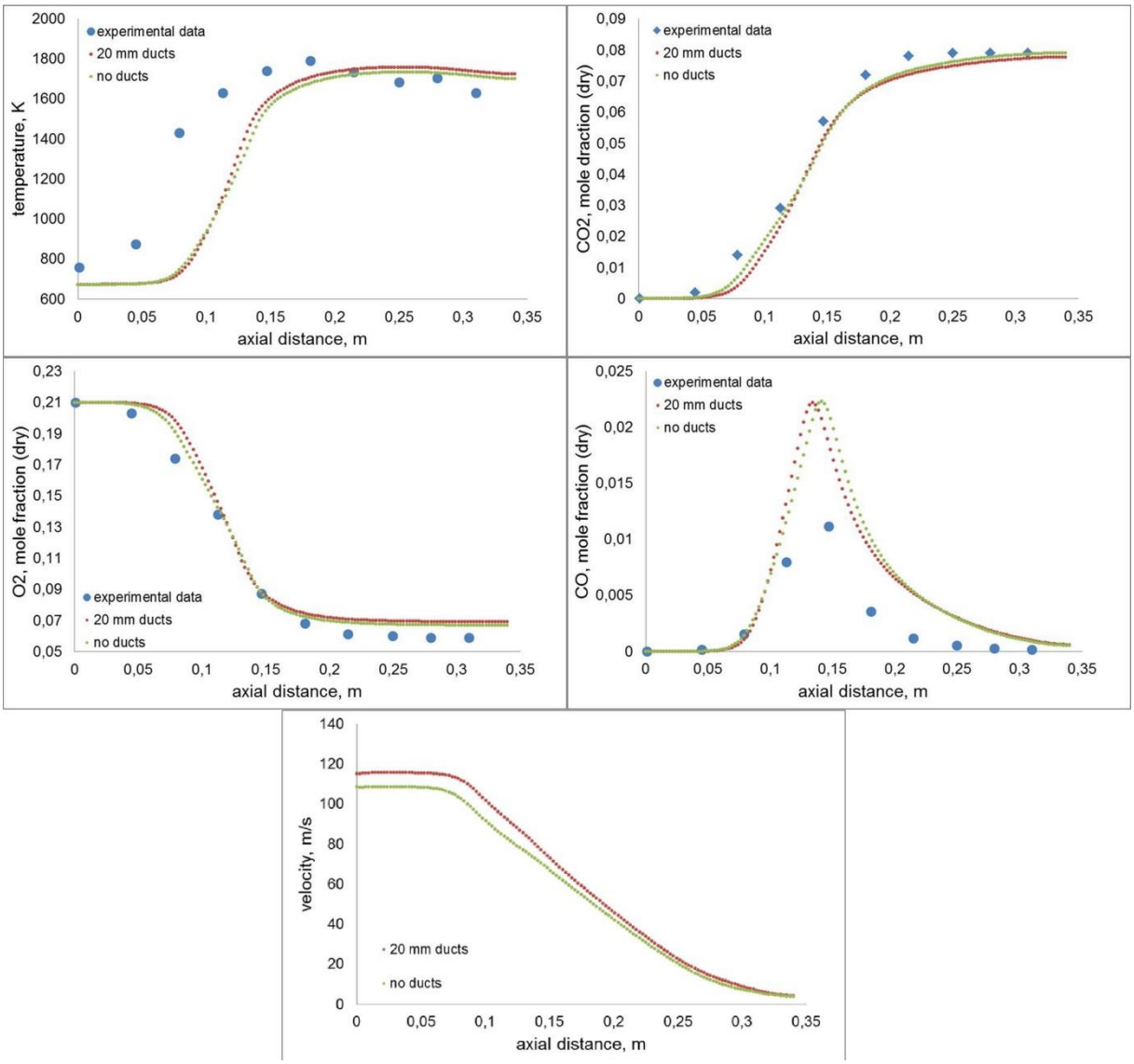

Fig. 5.3 Predicted and measured axial profiles of mean temperature, velocity, CO2, O2 and CO mean molar fractions on a dry basis.

As it can be seen in figure 5.3, the described geometrical change has a little impact on the axial profiles of temperature and CO_2, O_2, CO species concentrations. However, there are some differences in velocity profiles due to the development of the flow before the entrance to the combustion chamber. Although the influence of temperatures and species concentrations is relatively small, taking into consideration the noticeable difference in the axial velocity profile and negligible additional computational time required by geometry with ducts, the ducts were included in further simulations.

5.4. Turbulence Model Influence

In the past numerical studies conducted on the present small-scale combustor, for instance by Veríssimo et al. (2015) the applied turbulence model was the Realizable $k-\varepsilon$. In the present study a different model, namely SST $k-\omega$, was introduced. The computational power required by the two models is similar and theoretically the SST $k-\omega$ should provide better results in the studied case.

The purpose of this part is to verify if the new model provides more satisfactory results with the regard to experimental data.

Configuration A was tested. Meshing, all the settings, solution methods and discretization schemes for both models were exactly the same. The comparison is conducted for the axial velocity, temperature profiles and species concentrations of CO_2, O_2 and CO.

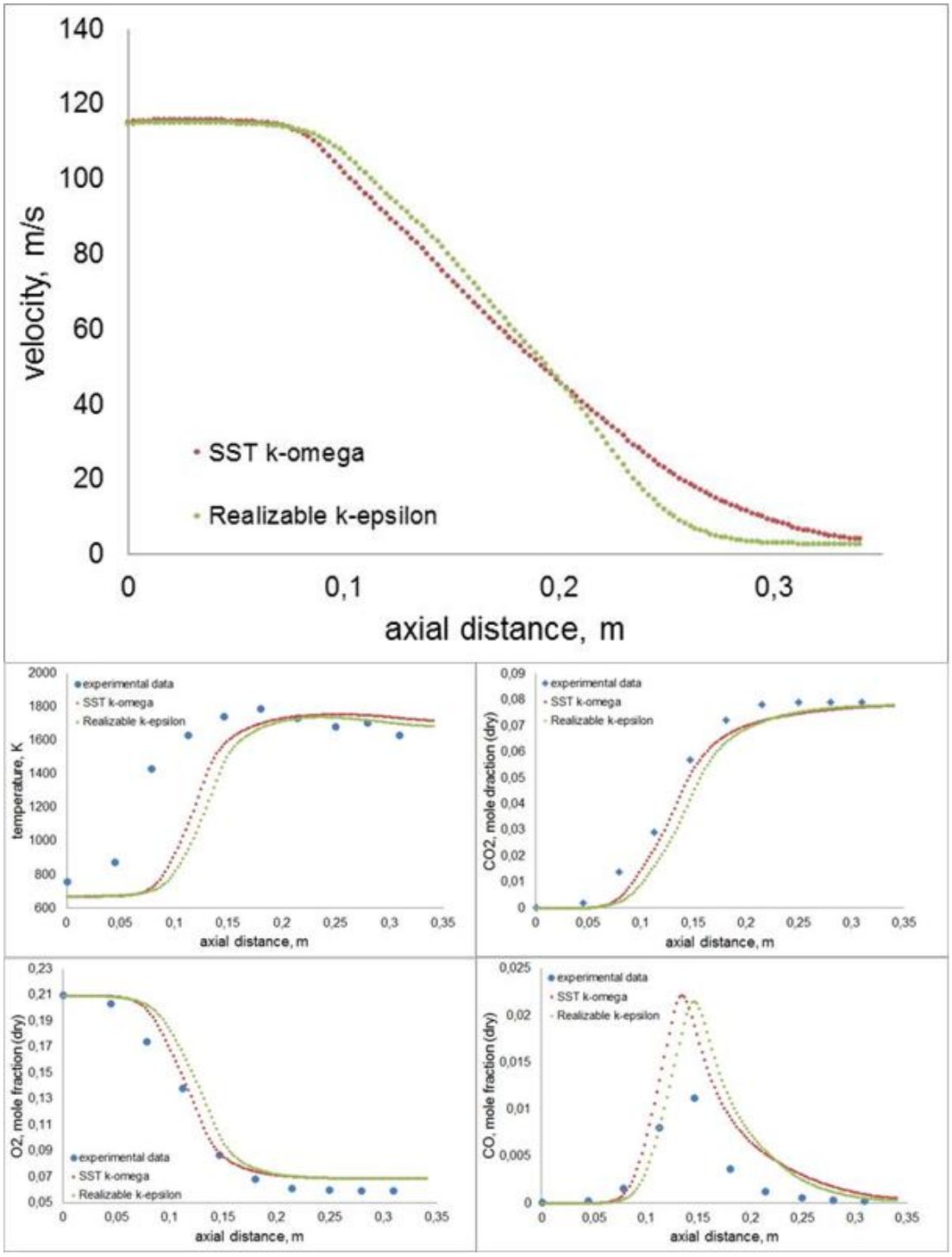

Fig. 5.4 Predicted and measured axial profiles of mean velocity, temperature, CO2, O2 and CO mean molar fractions on a dry basis.

As it was also observed in the previous numerical study (Veríssimo et al. 2015) the temperature prediction is underestimated. Both models fail to represent the initial decay of the inlet air stream and therefore, the reaction zone is moved away from the burner. The velocity profiles are very similar with relatively different results at the distance above about 200 mm, where the velocity drop is steeper for simulation with Realizable $k-\varepsilon$. Nevertheless, the simulation with SST $k-\omega$ model provides a more accurate prediction of the near-nozzle increase of temperature observed in the experiment. The predictions of CO2 and O2 concentrations are in fairly good agreement with the measurements with the indication of higher accuracy for SST $k-\omega$ model.

In the figure 5.5 the velocity fields for the two turbulence models are presented.

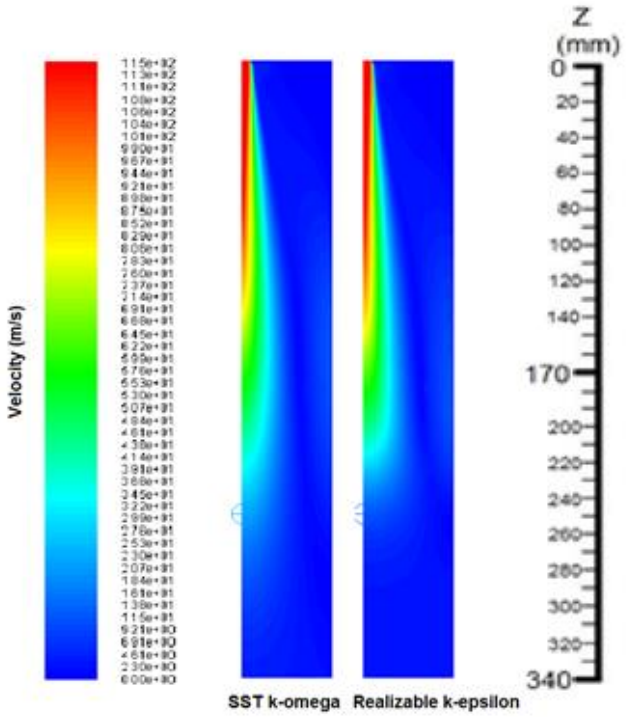

Fig. 5.5 Predicted velocity fields.

There are minor differences concerning the shape of the central air jet at the distance above 200 mm, between the velocity fields predicted with the simulations involving different turbulence models, which could also be deducted from the shape of the axial profiles, but overall, the fields are very similar.

5.5. Chemical Mechanism Influence

The chemical mechanism chosen for the purpose of this study is the reduced DRM-19 mechanism, described in chapter 3. The decision was based on the lower computational cost of such mechanism compared to the full mechanism GRI-1.2 and other more complex mechanisms. DRM-19 mechanism yields fewer variables comparing to its base full mechanism GRI-1.2 and this could have some impact on the results obtained with the two mechanisms. The purpose of this study is to assess the influence of using reduced over full mechanism in the given numerical problem.

Configuration A was tested and the turbulence model is SST $k-\omega$. The only difference between the two simulations is the chemical mechanism. The comparison is conducted for the axial temperature profiles and species concentrations of CO2, O2 and CO as presented in figure 5.5.

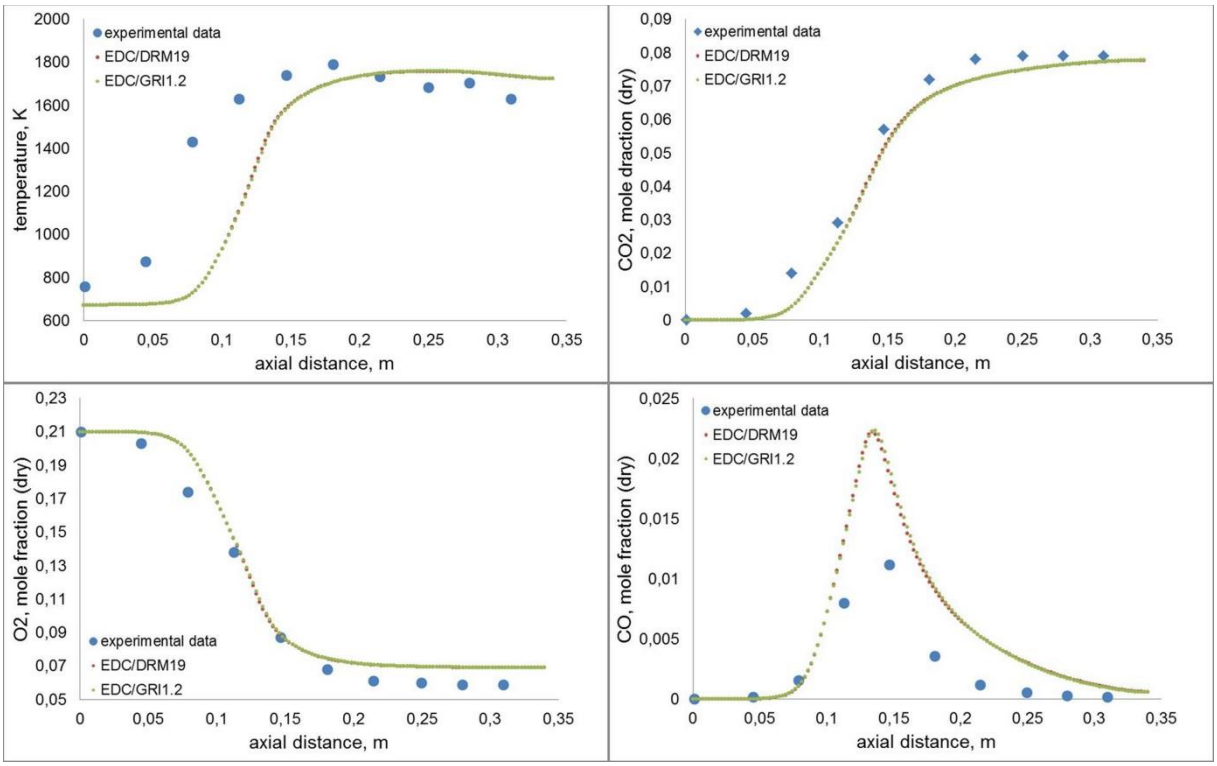

Fig. 5.6 Predicted and measured axial profiles of mean temperature, CO2, O2 and CO mean molar fractions on a dry basis.

The GRI-1.2 mechanism contains 32 species and 175 chemical reactions versus 21 species and 84 chemical reactions of the DRM-19 mechanism. Despite this difference, as can be concluded on the basis of the given axial profiles, the influence of using full over reduced mechanisms for the given case has practically no impact on the predictions of mean temperature and CO2, O2, CO mean concentrations.

5.6. Burner Configuration Study

In this part, the key simulations performed for the purpose of this Master Thesis are presented. The main objective is to determine in what way the different burner configurations affect the combustion process within the combustor designed to operate under flameless oxidation conditions. The burner configurations are presented in table 5.1. The predictions for configuration A will be compared with available experimental data, namely the measurements taken at points presented in chapter 2. For configurations A-E the OH* chemiluminescence images obtained in a research of Veríssimo et al. (2013) will be presented. The configurations F-K were neither tested experimentally nor numerically ever before.

Table 5.1 Simulated burner configurations with the corresponding number of mesh cells.

Configuration	Air inlet diameter D_{air} (mm)	Fuel inlet distance L (mm)	Number of mesh cells
A (available experimental data)	10	15	40 000
B	9	15	47 000
C	8	15	45 000
D	7	15	46 000
E	6	15	40 000
F	10	7.5	41 000
G	8	7.5	40 000
H	6	7.5	40 000
I	10	30	61 000
J	8	30	62 000
K	6	30	60 000

Test conditions for all the performed simulations are presented in detail in chapter 4 (table 4.5). The main characteristics of the tests are listed in table 5.2.

Table 5.2 Main test conditions.

Parameter	Value
Input power	10 kW
Excess air coefficient	1.3
Air inlet temperature	673 K
Air inlet velocity	Configurations: A, F, I – 108.47 m/s B – 133.92 m/s C, G, J – 169.49 m/s D – 221.37 m/s E, H, K – 301.31 m/s
Air inlet diameter	Configurations: A, F, I - 10 mm B - 9 mm C, G, J - 8 mm D - 7 mm E, H, K - 6 mm
Air inlet species (mole fraction)	0.21 O_2 0.79 N_2
Air inlet turbulence specification	Turbulent intensity - 5 % Hydraulic diameter = Air inlet diameter
Fuel inlet temperature	298 K
Fuel inlet velocity	6.06 m/s

Fuel inlet diameter	2 mm
Fuel inlet species (mole fraction)	1 CH_4

On the foundation of past experimental studies performed on the small-scale combustor (Veríssimo et al. 2011) and on the basis of the fundamental knowledge gained from literature, the nature of the flow should be explained to gain a better understanding of the presented results. The momentum of the central air jet is large enough to generate a strong reverse flow zone, that recirculates hot flue gas back toward the near-burner region so that the combustion occurs under relatively low oxygen concentrations, which are required to sustain the flameless combustion regime. The central air nozzle momentum is the main driver for the establishment of the desired, flameless combustion regime. In figure 5.6, the idealized scheme of the flow within the combustor is presented.

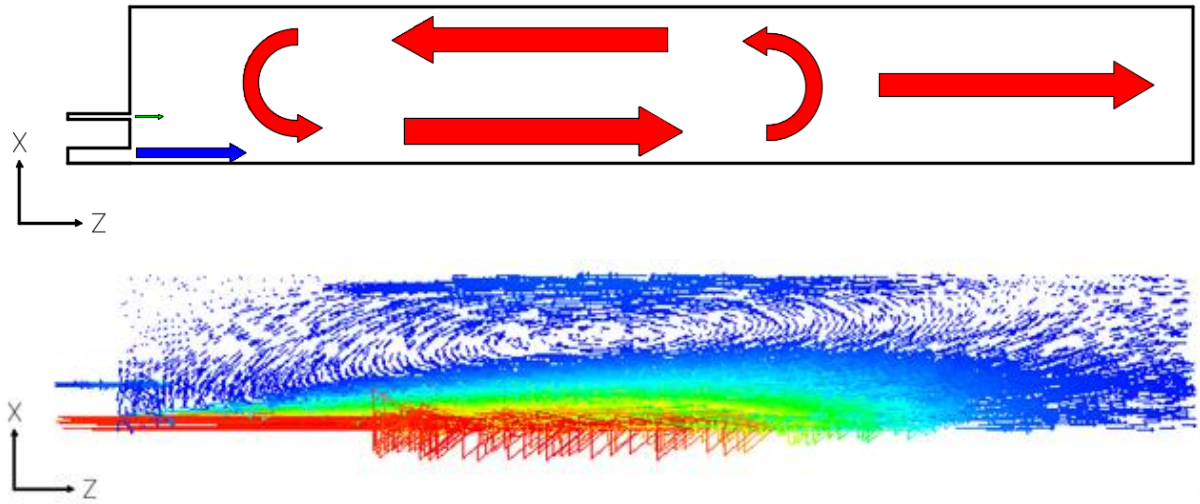

Fig. 5.7 Idealized scheme of the flow (top) and Fluent velocity vectors (bottom).

Initially, the graphs of axial profiles of temperature, velocity and CO2, O2, CO concentrations are presented in figures 5.7-9. Subsequently, the contours of mean temperature and mean OH concentration contours are presented in figures 5.10-13. The mean OH predictions are compared with the available OH* images obtained in the experimental study of Veríssimo et al. (2013). At last, the maximum temperatures, average (weighted by volume) temperatures and average temperature deviation (weighted by volume) predicted in all the simulations are listed in table 5.3.

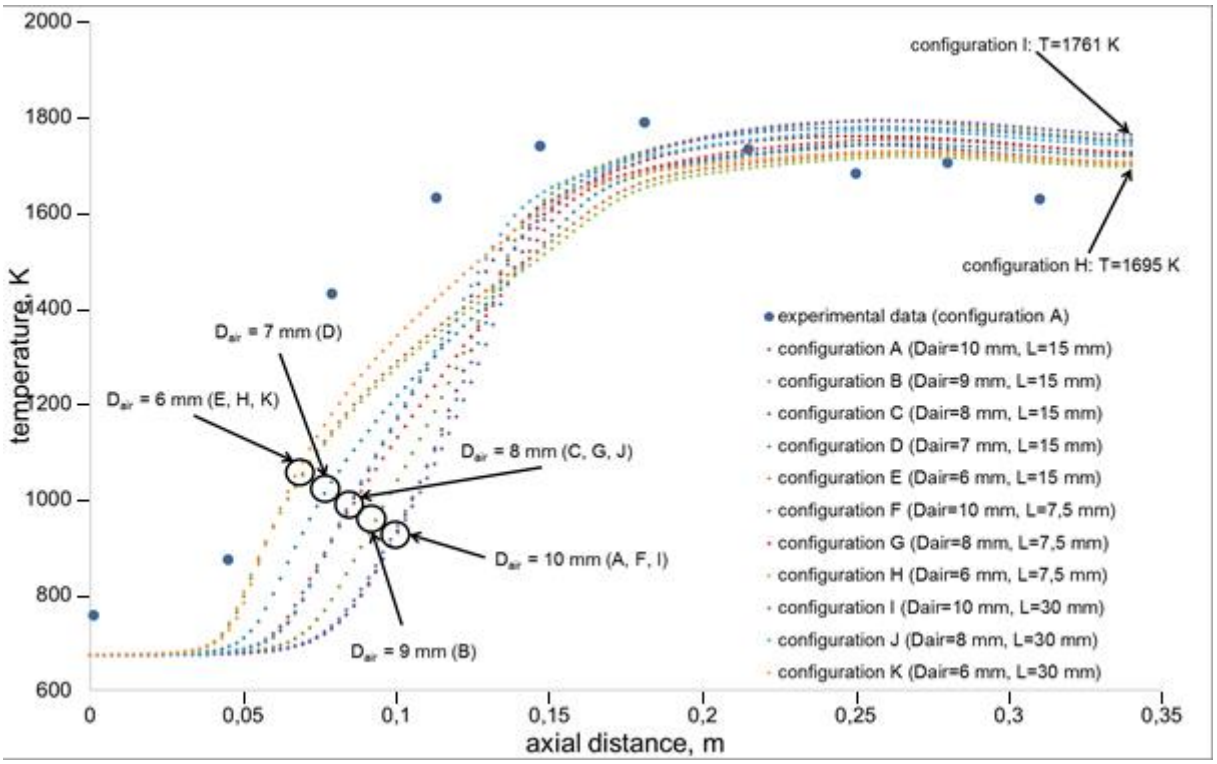

Fig. 5.8 Predicted and measured axial profiles of mean temperature.

The predictions of axial mean temperature profiles for all the tested configurations reveal, that for burner configurations with smaller inlet air diameter, the decay of the jet occurs quicker and therefore, the main reaction zone and corresponding temperature rise are observed closer to the burner. Despite the relatively large difference in air velocity (301,31 m/s for D_{air} = 6 mm and 108,47 m/s for D_{air} = 10 mm) and different fuel inlet distance L, the temperature profiles for axial distance over z ≈ 0.15 m are relatively close for all the configurations, which indicates, that the main reaction zone is up to ≈ 0.15 m. The highest and lowest axial temperatures at the outlet are observed for the most extreme configurations, namely I (D_{air} = 10 mm, L = 30 mm) and H (D_{air} = 6 mm, L = 7,5 mm). The reason for this is that for the configuration I, the main reaction zone is further away from the burner, opposite to the configuration H, where the reaction zone (and the related temperature increase) is closer to the burner. This indicates, that the mixing between fuel and oxidizer is slower for configurations with larger values of L and lower air inlet velocities. The shapes of the profiles at an axial distance from z ≈ 50 mm z ≈ 150 mm reveal, that the initial increase of temperature is mostly dependent on air inlet diameter, because despite different values of fuel inlet distances L, the profiles with equal values of D_{air} clearly coincide, what is marked in the graph.

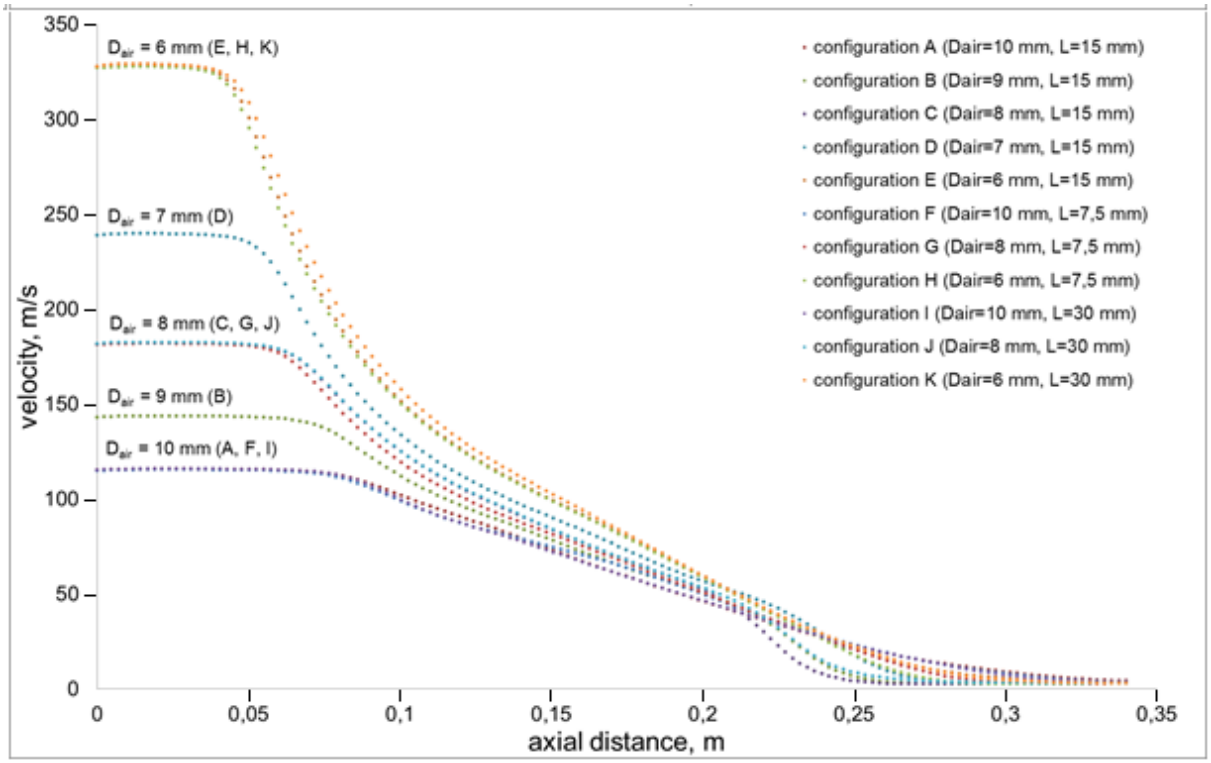

Fig. 5.9 Predicted axial profiles of mean velocity.

The axial velocity profiles for different configurations show that the velocity decreases more rapidly for higher inlet velocities (or for smaller air inlet diameters). Furthermore, it can be observed, that the decay of the jet occurs closer to the burner for higher inlet velocities. The profiles are closer to each other as the distance from the burner increases above z ≈ 100 mm.

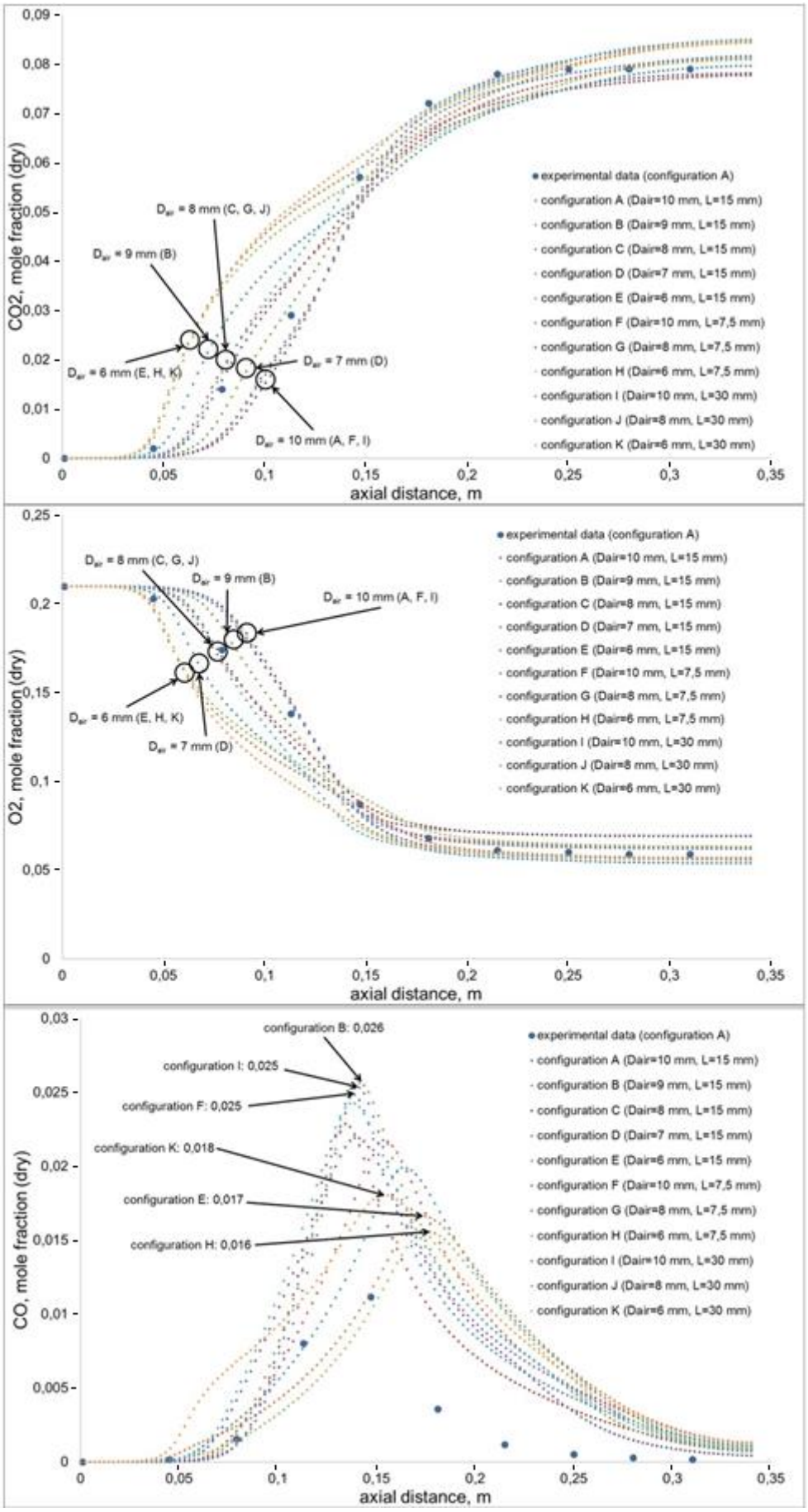

Fig. 5.10 Predicted and measured axial profiles of CO2, O2, and CO mean molar fractions on a dry basis.

It is observed, that, when it comes to the axial profiles of CO_2 and O_2 concentrations, the biggest impact on the profiles is related to the air inlet diameter. For smaller diameters, the inlet velocity is larger and the decay of the jet, as well as the main reaction zone, move closer to the burner, which could also be concluded from the temperature and velocity profiles. The mean CO molar fraction profiles overestimate the experimental data. Nevertheless, the qualitative prediction is satisfactory, the peak concentration is expected in the similar region, as in experimental measurements. Comparing the predictions for different burner configurations it can be observed, that the lowest peak concentrations are expected for configurations with the smallest air inlet diameter, which can be related to more intense mixing between the oxidizer, fuel and recirculated flue gas for larger air inlet velocities. Furthermore, the lowest peak concentration was predicted for configuration H, where the air and fuel jets are very close to each other, meaning that the fuel stream is quickly sucked by the air stream and reaction takes place faster and with higher oxygen concentration. The highest peak CO concentrations were predicted for configurations with D_{air} equal to 10 and 9 mm (B, F and I).

In figures 5.10-11 the contours of temperature and OH species fields are presented for all tested configurations. The OH is an important intermediate species present in the combustion process of hydrocarbon fuels, like methane. High OH concentrations can be correlated with the high intensity of reaction in the given region and therefore it provides a valuable source of information concerning the nature of the combustion process. More uniform temperature and OH fields are related to the flameless combustion regime, while the presence of regions of very high temperature and OH concentrations signalize the appearance of flame front related to regular combustion regime.

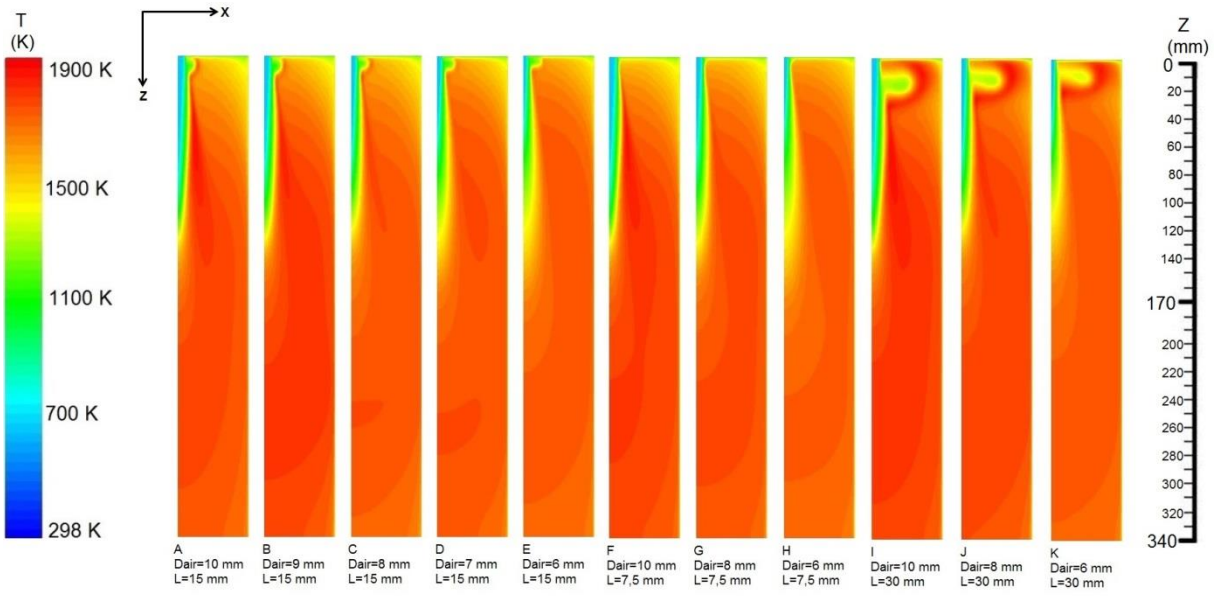

Fig. 5.11 The contours of predicted temperature fields for all tested configurations.

The temperature fields of configurations A-E reveal that with the decrease of the air inlet diameter and higher air inlet velocity lead to more uniform temperature field and absence of high temperature regions, which could indicate the presence of flame front. For configurations A-E there is a zone of

higher temperature near the burner between z ≈ 0 to 20 mm, and along the inlet air jet between z ≈ 30 mm to 150 mm, which becomes more stretched and cooler for higher air inlet velocities. The region between z ≈ 0 to 20 mm disappears for configurations F-G, which are also the configurations, where the temperature field is the most uniform. When comparing all the configurations it is clear that the combination of the lower air inlet diameter with smaller air fuel inlets distance produces the most uniform temperature field, which can be proven by the temperature field observed in configuration H having the smallest tested air inlet diameter and the smallest distance between the air and the fuel nozzles. The configurations I-K, with a distance of 30 mm yields the least uniform temperature fields with clearly visible high temperature regions, which could indicate the presence of a flame front between z ≈ 0 to 40 mm and along the air jet between z ≈ 30 mm to 150 mm.

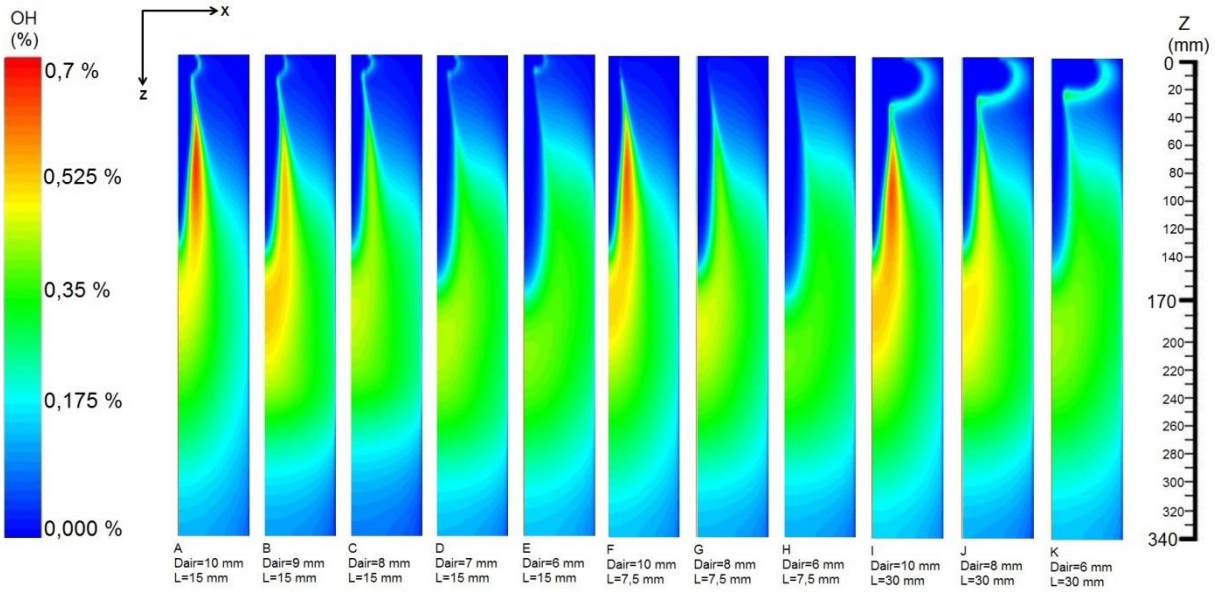

Fig. 5.12 The contours of predicted OH fields for all tested configurations.

By the OH concentration fields of configurations A-E it can be observed that with increasing air inlet velocity, the combustion process occurs at a larger region and closer to the burner, which indicates, that the intensity of recirculation is correlated with the air jet momentum. The consequence of this is that the reactions are less intense, the region of high OH concentration visible for configuration A is distributed over a larger region for configurations with lower air inlet diameter B-E. This region, marked in different shades of red, is visible for configurations with the air inlet diameter of 10 mm, namely A, F and I. Again, as formerly deducted from the temperature fields, the reaction zone is more uniform for lower air fuel inlet distances, this can be seen for example in the OH fields F-H, where the value of L is equal to 7,5 mm. The best configuration concerning the flameless combustion regime was achieved for configuration H, where both temperature and OH concentrations turned out to be mostly uniform over the whole simulated combustion chamber.

As mentioned before, thanks to the experimental research on small-scale combustor performed by Veríssimo et al. (2013), there are available temperature fields for burner configuration A and D and OH

fields for configurations A-E. These fields are presented in figures 5.12-13 and compared with the predictions gathered in numerical simulations. The comparison is treated qualitatively and concerns the distribution of temperature and OH concentration within the combustion chamber.

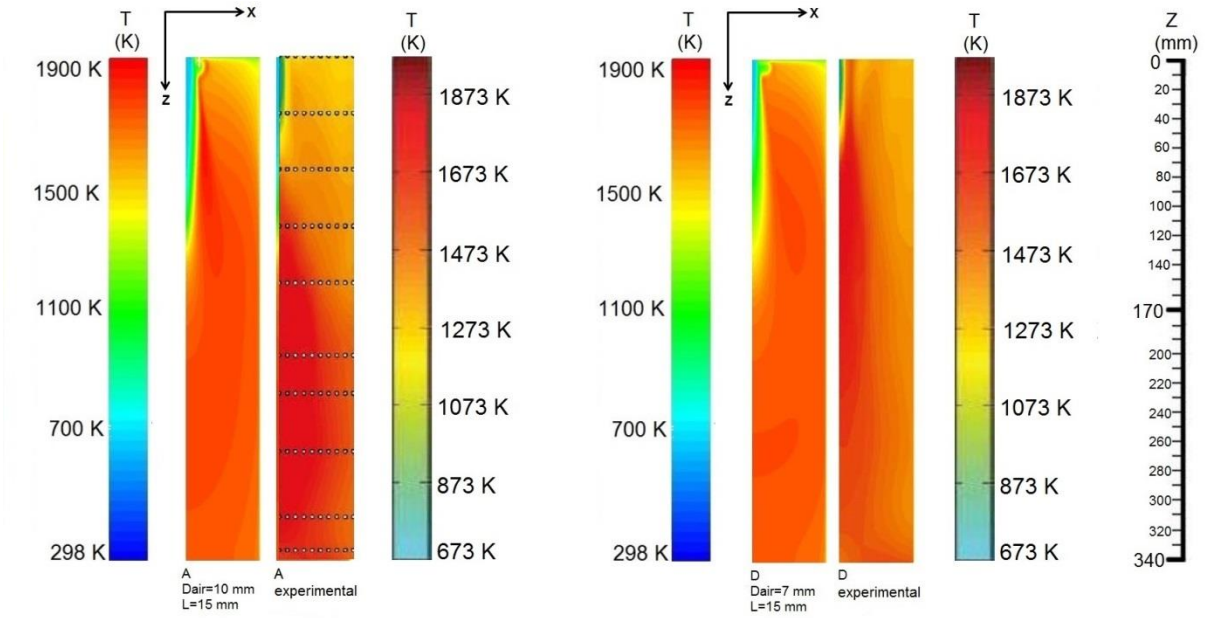

Fig. 5.13 The temperature field predictions combined with obtained experimentally for configurations A and D (Veríssimo et al. 2013).

The contours of predicted and measured temperature confirm the observations made on the basis of axial temperature profiles. The simulations fail to predict the initial decay of the central jet and the increase of temperature observed in the experiment. Nevertheless, excluding the region near the axis between z ≈ 0 mm and z ≈ 140 mm, the predicted temperature distribution is in good agreement with the experimental data over the major area of the combustor for presented configurations A and D. The experimental temperature field for configuration D validates the conclusion made on the basis of predicted temperature fields, that with increasing air jet momentum, the temperature is more uniform over the whole combustion chamber.

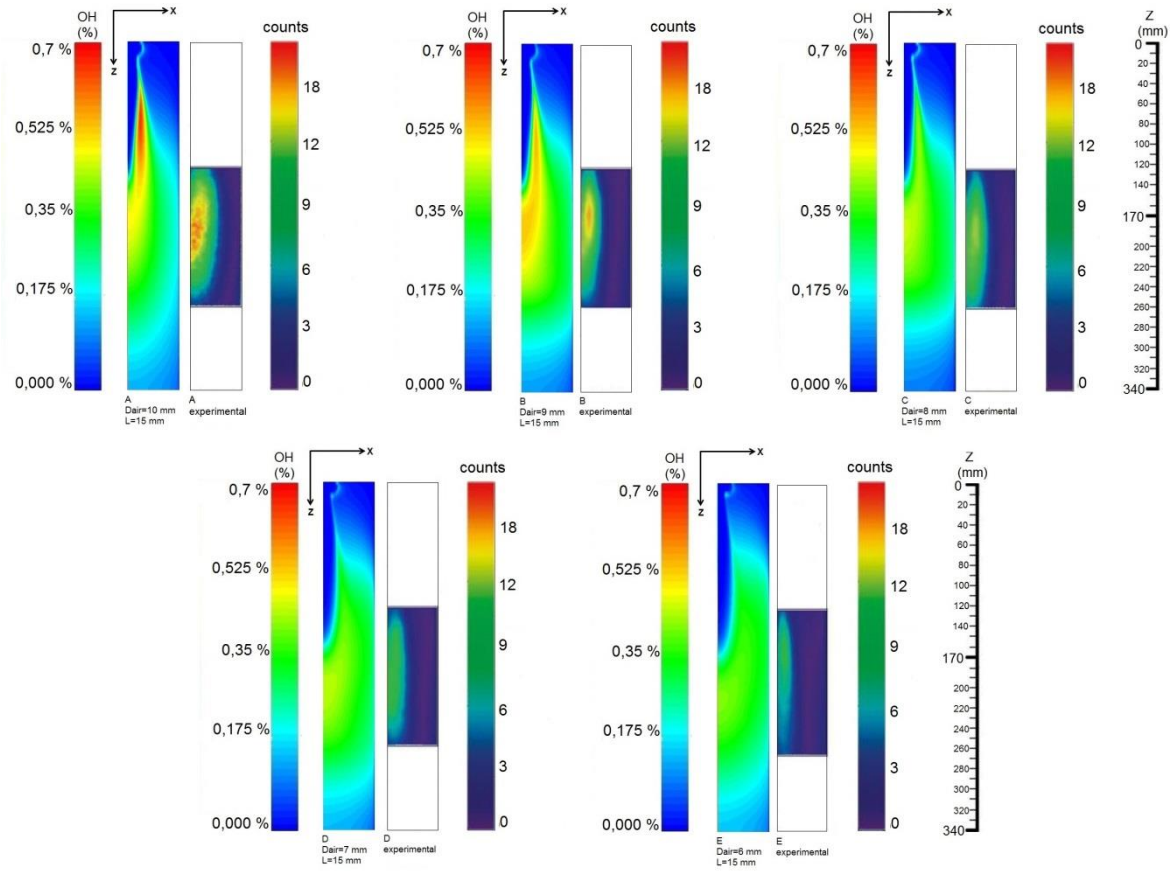

Fig. 5.14 The OH field contours combined with OH* images obtained in the experiment for configurations A-E (Veríssimo et al. 2013).

It needs to be noted that, due to the short lifetime of OH*, the chemiluminescence originates only from the reaction zone so that the chemiluminescence imaging technique yields information about the position and size of the reaction zone (Lee and Santavicca 2003). In configuration A, the region with highest OH concentration is predicted closer to the burner between z ≈ 40 mm and z ≈ 120 mm, in comparison to the OH* image. Nevertheless, the location of the main reaction zone is in fair agreement with the experimental data. For configurations B-E, both predicted and measured OH contours show that the main reaction zone is observed in the region between z ≈ 120 mm and z ≈ 240 mm. As the air inlet velocity increases, both predicted and measured OH intensities decrease, which indicates higher entrainment of the reacting mixture.

In table 5.3 the maximum temperatures T_{max}, average temperatures T_{avg} (by volume) and average temperature deviations T* (by volume) are listed. The average temperature deviation is given by:

$$T^* = \frac{|T_{max} - T_{avg}|}{T_{avg}} \tag{5.6-1}$$

Table 5.3 The comparison of maximum, average temperatures and temperature deviations for the tested configurations.

Configuration:	T_{max}, K:	T_{avg}, K:	T*:
A	1871	1688	0.109
B	1819	1714	0.061
C	1794	1681	0.067
D	1747	1691	0.033
E	1748	1681	0.040
F	1851	1708	0.084
G	1759	1696	0.037
H	1727	1677	0.030
I	1890	1730	0.093
J	1896	1720	0.103
K	1883	1694	0.111

From the presented data, it can be noticed that, with the exception of configuration B, the lower the air inlet diameter (and therefore higher air jet momentum), the maximum and average temperature decreases, which means that there is stronger recirculation between the flue gas and the reactants producing more leveled temperature field. The same correlation can be found for the fuel inlet nozzle distance L, as the highest peak and average temperatures are noted for the highest distance of L = 30 mm and the lowest for the distance of L = 7,5 mm. The configuration H yields the lowest values of these parameters and also the lowest value of average temperature deviation. These values for configuration H are the most favorable results when it comes to the establishment of the flameless combustion regime, and it can be expected that this configuration would produce the lowest emission of thermal NO_x.

Velocity profiles in near burner region of configurations H and K yielding the lowest and the highest temperature deviations can be assessed in the appendix, Fig. 1 and Fig. 2. These velocity profiles are helpful in the understanding of the differences between predictions obtained with these two configurations.

Chapter 6

Conclusions and Future Work

6.1. Conclusions

The numerical simulations of a small-scale combustor operating in the flameless combustion regime were conducted. The main objective of the work was to evaluate the impact of the geometrical changes of the burner, namely the diameter of the air nozzle and the distance between the air and fuel nozzles on the combustion process. In order to optimize the setup for simulations with modified burner geometry, initially, the grid independence study was performed followed by the geometry influence, turbulence model influence, and chemical mechanism influence studies. The turbulence model was SST $k-\omega$ and the species transport model was EDC coupled with the detailed chemical mechanism DRM-19 containing 21 species and 84 reactions.

As a result of the grid independence study, the grid of approximately 40 000 elements turned out to produce satisfactory results comparing to experimental data and with negligible difference comparing to grids of 136 000 and 352 000 elements. Having in mind the lower computational time related with such grid, comparing to finer grids, it was chosen as the base grid for further simulations.

The basis of the geometry influence study was to evaluate the impact of using a geometry with inlet ducts and without inlet ducts. The comparison showed that the difference between the two geometries was negligible when it comes to axial profiles of mean temperature and CO_2, O_2 and CO concentrations, but there was a noticeable difference in the predictions of the mean axial velocity. For this reason, and due to the fact that the computational time difference required by the two geometries was insignificant, the decision was made to progress with the complete geometry.

Turbulence models applied in the comparison were SST $k-\omega$ and realizable $k-\varepsilon$. Both models are not accurate to predict the initial decay of air inlet jet, which was observed in the experimental work on small-scale combustor. Nevertheless, the SST $k-\omega$ model produces more accurate predictions than realizable $k-\varepsilon$, without noticeable increase in the required computational time. Therefore the SST $k-\omega$ turbulence model was employed in the following simulations.

The DRM-19 mechanism was chosen due to its simplicity. It is a reduced mechanism based on the full mechanism GRI-1.2. The study was made in order to evaluate the influence of using reduced over full mechanism on the results. The conclusion is that, for the given problem, the DRM-19 mechanism produces almost the same results as the more complex and more computationally demanding mechanism GRI-1.2.

All 11 different burner configurations (A-K) were simulated. For configurations A-E, the predictions were compared with experimental data drawn from past studies of Veríssimo et al. (2011 and 2013). In order to evaluate the impact of geometrical changes of air nozzle diameter and fuel nozzle distance on the combustion process. The conclusions are as follows:

- Changing the air inlet diameter at constant excess air coefficient and constant power level induces the change in air inlet velocity. For smaller air inlet diameter (and thus higher air inlet velocity) the decay of the air jet occurs quicker, which is shown by mean temperature and mean velocity axial profiles
- With smaller air inlet diameters the main reaction zone moves closer to the burner region due to more intense entrainment of the gas mixture
- The CO concentrations are overpredicted comparing to experimental data, however, the peak concentrations are in good agreement with the measurements, meaning that the maximum concentration is located in the similar region of the combustor. The lowest peak CO concentrations are observed for configurations with the smallest fuel inlet distance, namely F, G, H with the lowest predicted CO concentration for configuration H (D_{air} = 6 mm, L = 7,5 mm)
- By the temperature contours, OH contours and the information about a maximum temperature, an average temperature, and an average temperature deviation, it is predicted that the most uniform temperature field and lowest maximum temperature is expected for configuration H, which combines the smallest tested air inlet diameter with the lowest tested air fuel inlet distance; the general trend was noticed, that the temperature and OH fields are more uniform by both lower air inlet diameter and lower air fuel inlet distance
- For configurations I-K (D_{air} = 10, 8, 6 mm, L = 30 mm) high temperature and OH regions were predicted, which may mean the presence of flame front, which is not desired in the context of achieving flameless oxidation regime
- The most favorable predictions for the achievement of flameless oxidation regime are for burner configurations with fuel inlet distance of 7.5 mm preferably combined with air inlet diameter of 6 mm as in configuration H

6.2. Future Work

The following suggestions for future work are proposed:

- Experimental study on combustion characteristics on small-scale combustor operating with burner geometry of configurations F-H, that turned out to perform the best in context of flameless oxidation combustion regime
- Use of more advanced turbulence model, so that the initial decay of air jet is accurately predicted with regard to experimental results

References

Cavaliere A., and Joannon M. (2004). Mild Combustion. Progress in Energy and Combustion Science, **30**, pp. 329-366.

Christo F.C., Dally B. B. (2005). Modeling turbulent reacting jets issuing into a hot and diluted coflow. Combustion and Flame, **142**, pp. 117-129.

Coppalle A. and P. Vervisch. (1983). The Total Emissivities of High-Temperature Flames, Combustion and Flame, **49**, pp. 101–108.

FLUENT Theory Guide (2016). Version 17.1. Lebanon, NH: ANSYS Inc.

FLUENT User's Guide (2016). Version 17.1. Lebanon, NH: ANSYS Inc.

Frenklach M., H. Wang, M. Goldenberg, G.P. Smith, D.M. Golden, C.T. Bowman, R.K. Hanson, W.C. Gardiner and V. Lissianski (1995). GRI-Mech---An Optimized Detailed Chemical Reaction Mechanism for Methane Combustion, Report No. GRI-95/0058.

Graça M., A. Duarte, P.J. Coelho and M. Costa (2012), Numerical simulation of a reversed flow small-scale combustor, Fuel Processing Technology, **107**, pp. 126-137.

Hosseini S. E., G. Bagheri, M. A. Wahid (2014). Numerical investigation of biogas flameless combustion, Energy Conversion and Management, **81**, pp. 41-50.

https://www.eia.gov/tools/faqs/faq.cfm?id=74&t=11 (access: October 2016)

https://www.intechopen.com/source/html/45115/media/image13.png (access: October 2016)

http://www.engineeringtoolbox.com/dry-air-properties-d_973.html (access: October 2016)

Kazakov A. and M. Frenklach, http://www.me.berkeley.edu/drm/

Katsuki M. and T. Hasegawa, T. (1998). The Science and Technology of Combustion in Highly Preheated Air, **27(2)**, pp. 3135-3146.

Key world energy statistics (2016). International Energy Agency (IEA).

Krishnamurthy, N., Paul, P.J., and Blasiak, W. (2009). Studies on low-intensity oxy-fuel burner. Proc. Combust. Inst., **32**, pp. 3139–3146.

Kumar, S., Paul, P.J., and Mukunda, H.S. (2002). Studies on a new high-intensity low-emission burner. Proc. Combust. Inst., **29**, pp. 1131–1137.

Launder, B.E. and Spalding D.B. (1974). The numerical computation of turbulent flows, Comp Meth Appl Mech Eng, **3**, pp. 269-289.

Lee J.G., D.A. Santavicca (2003). Experimental diagnostics for the study of combustion instabilities in lean premixed combustors, J. Propul. Power **19**, pp. 735–750.

Magnussen B. F. (1981). On the Structure of Turbulence and a Generalized Eddy Dissipation Concept for Chemical Reaction in Turbulent Flow, Nineteenth AIAA Meeting, **3**, pp. 269-289.

Magnussen, B. F. (1989). Modeling of pollutant formation in gas turbines combustors based on the eddy dissipation concept. 18th International Congress on Combustion Engines, International Council on Combustion Engines, Tianjin, China.

Menter F. R. (1993). Two-Equation Eddy-Viscosity Turbulence Models for Engineering Applications, AIAA Journal, **32(8)**, pp. 1598-1605.

Mi, J., Li, P., Dally, B.B., and Craig, R.A. (2009). Importance of initial momentum rate and air-fuel premixing on moderate or intense low oxygen dilution (MILD) combustion in a recuperative furnace. Energy Fuels, **23**, pp. 5349–5356.

Noor M.M., Andrew P., Wandel, and Talal Yusaf (2012). A Review of Mild Combustion and Open Furnace Design Consideration, **6**, pp. 730-754.

Pope S. B. (1997). Computationally efficient implementation of combustion chemistry using in situ adaptive tabulation, Combustion Theory and Modelling, **1**, pp. 41-63.

Shih, T. H., Liou, W. W., Shabbir, A., Yang, Z., e Zhu, J. (1995). A new *k*-ε eddy-viscosity model for high Reynolds number turbulent flows – model development and validation. Computers Fluids, **24**, pp 227-238.

Smith T. F., Z. F. Shen, and J. N. Friedman (1982). Evaluation of Coefficients for the Weighted Sum of Gray Gases Model, J. Heat Transfer, **104**, pp. 602–608.

Veríssimo A. S., A. M. Rocha A., and Costa M., M. (2011). Operational, Combustion, and Emission Characteristics of a Small-Scale Combustor, Energy Fuels, **25**, pp. 2469-2480.

Veríssimo A.S., A.M.A. Rocha and M. Costa, M. (2013). Experimental study on the influence of the thermal input on the reaction zone under flameless oxidation conditions, Fuel Processing Technology, **106**, pp. 423–428.

Veríssimo A.S., A.M.A. Rocha and M. Costa, M. (2013). Importance of the inlet air velocity on the establishment of flameless combustion in a laboratory combustor, Experimental Thermal and Fluid Science, **44**, pp. 75–81.

Veríssimo A. S., A. M. A. Rocha, P. J. Coelho and M. Costa, M. (2015). Experimental and Numerical Investigation of the Influence of the Air Preheating Temperature on the Performance of a Small-Scale Mild Combustor, Combustion Science and Technology, **187(11)**, pp. 1724-1741.

Wünning, J. A. and Wünning, J. G. (1997). Flameless oxidation to reduce thermal NO-formation. Progress Energy Combustion Science, **23**, pp. 81-94.

Wünning, J. A. and Wünning, J. G. (2001). Ten years of flameless oxidation technical application and potentials. 4th HTAC High Temperature Air Combustion, November, Rome.

Appendix

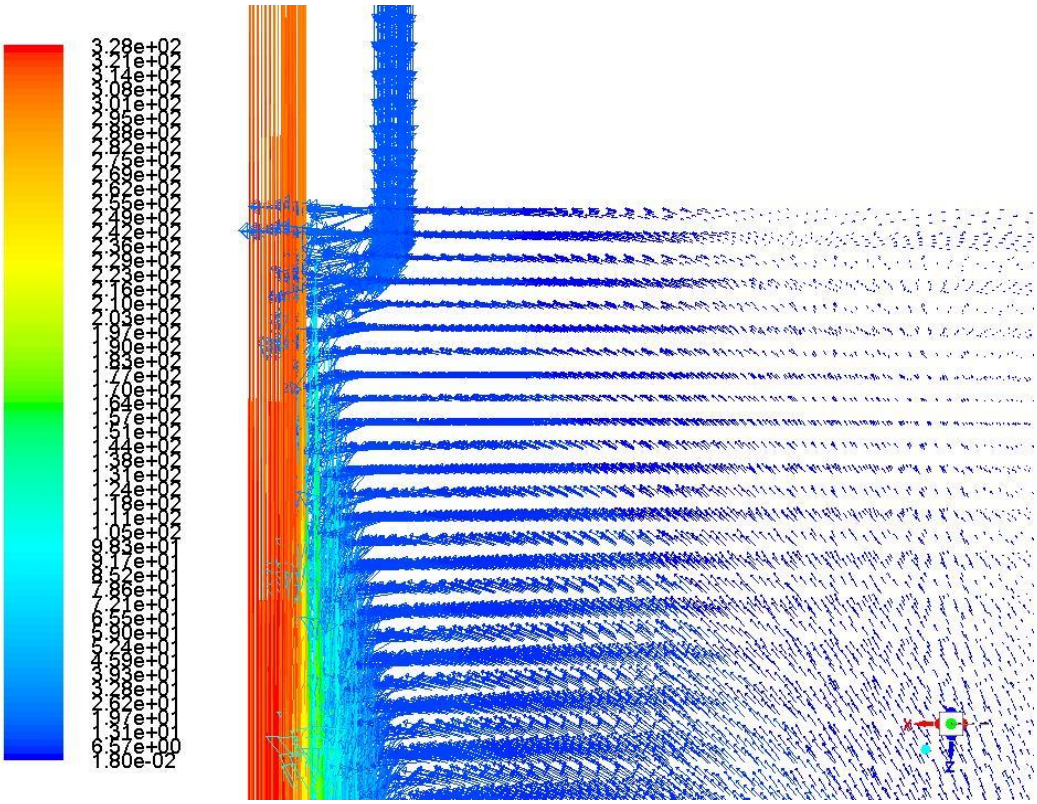

Fig. 1 Velocity profile of configuration H (vectors scale - 100:1).

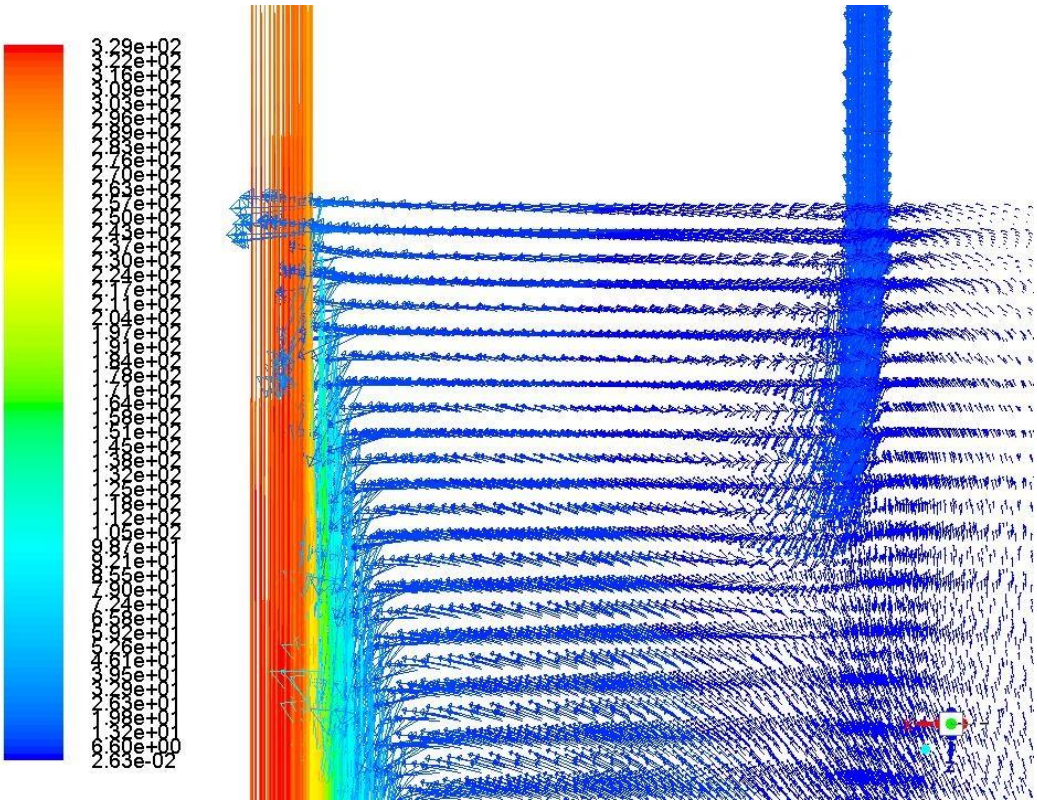

Fig. 2 Velocity profile of configuration K (vectors scale - 100:1).